Biomaterials 316 (2025) 123009

Contents lists available at ScienceDirect

Biomaterials

journal homepage: www.elsevier.com/locate/biomaterials

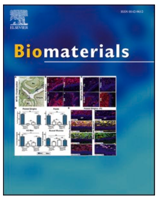

A bioprinted and scalable model of human tubulo-interstitial kidney fibrosis

Daphne Bouwens [a,1], Nazanin Kabgani [a,1], Cédric Bergerbit [d,e,2], Hyojin Kim [a,2], Susanne Ziegler [a], Sadaf Ijaz [a], Ali Abdallah [b], Tamás Haraszti [c,d], Sidrah Maryam [a], Abdolrahman Omidinia-Anarkoli [d,e], Laura De Laporte [c,d,e], Sikander Hayat [a], Jitske Jansen [a], Rafael Kramann [a,f,*]

[a] Department of Medicine 2 (Nephrology, Rheumatology, Clinical Immunology, Hypertension), RWTH Aachen University Medical Faculty, Aachen, Germany
[b] Interdisciplinary Center for Clinical Research, RWTH University Aachen, Germany
[c] ITMC-Institute for Technical and Macromolecular Chemistry, RWTH Aachen University, Aachen, Germany
[d] DWI–Leibniz Institute for Interactive Materials e.V., Aachen, Germany
[e] AMB–Advanced Materials for Biomedicine, Institute of Applied Medical Engineering, University Hospital Aachen, Germany
[f] Department of Internal Medicine, Nephrology and Transplantation, Erasmus Medical Center, Rotterdam, the Netherlands

ARTICLE INFO

Keywords:
Chronic kidney disease
Kidney fibrosis
Myofibroblasts
Bioprinting
Extracellular matrix

ABSTRACT

Chronic kidney disease (CKD) affects more than 10% of the global population. As kidney function negatively correlates with the presence of interstitial fibrosis, the development of new anti-fibrotic therapies holds promise to stabilize functional decline in CKD patients. The goal of the study was to generate a scalable bioprinted 3-dimensional kidney tubulo-interstitial disease model of kidney fibrosis. We have generated novel human PDGFRβ$^+$ pericytes, CD10$^+$ epithelial and CD31$^+$ endothelial cell lines and compared their transcriptomic signature to their *in vivo* counterpart using bulk RNA sequencing in comparison to human kidney single cell RNA-sequencing datasets. This comparison indicated that the novel cell lines still expressed kidney cell specific genes and shared many features with their native cell-state. PDGFRβ$^+$ pericytes showed three-lineage differentiation capacity and differentiated towards myofibroblasts following TGFβ treatment. We utilized a fibrinogen/gelatin-based hydrogel as bioink and confirmed a good survival rate of all cell types within the bioink after printing. We then combined all three cells in a bioprinted model using separately printed compartments for tubule epithelium, and interstitial endothelium and pericytes. We confirmed that this 3D printed model allows to recapitulate key disease driving epithelial-mesenchymal crosstalk mechanisms of kidney fibrosis since injury of epithelial cells prior to bioprinting resulted in myofibroblast differentiation and fibrosis driven by pericytes after bioprinting. The bioprinted model was also scalable up to a 96-well format.

1. Introduction

Chronic kidney disease (CKD) is a pandemic that already affects over 10 % of the population worldwide. Once CKD progresses towards end stage renal disease (ESRD), patients need to undergo dialysis or transplantation. While transplantation waiting times number in years due to the worldwide shortage of organ donor supply, dialysis is associated with a tremendous morbidity and mortality. Furthermore, CKD and ESRD have a tremendous societal impact as evident in the form of substantial costs and the loss of productivity [1,2]. Tubulointerstitial kidney fibrosis is a hallmark of CKD and therefore considered an important therapeutic target. Despite this, currently no kidney-specific antifibrotic therapy exists. In addition, while the human kidney is complex and consists of various cell types with high architectural and physiological complexity, the current screening systems for target validation or new therapeutic compounds are primarily based on monolayer 2-dimensional (2D) cell-culture. Monolayer cell culture studies are artificial and not comparable to a 3-dimensional (3D) tissue where

---

[*] Corresponding author. Department of Medicine 2 RWTH Aachen University, Medical Faculty Pauwelsstrasse 30, 52074, Aachen, Germany.
E-mail address: rkramann@gmx.net (R. Kramann).

[1] Both authors contributed equally.

[2] Shared senior authors.

https://doi.org/10.1016/j.biomaterials.2024.123009
Received 25 April 2024; Received in revised form 11 December 2024; Accepted 11 December 2024

cell-cell and cell-matrix interactions are crucial in many disease processes. While animal experiments would provide a more representative environment to model kidney disease, translational concerns remain due to the interspecies differences, which explain why so many promising preclinical drug candidates fail in early clinical trials [3]. Furthermore, animal models are not a suitable screening platform that would allow for testing of hundreds to thousands of compounds. In addition, ethical concerns regarding *in vivo* experiments stimulate the development of new representative human kidney disease models. Current advanced *in vitro* models include induced pluripotent stem cell (iPSC)-derived kidney organoids and Kidney-On-A-Chip microfluidic models. While iPSC-derived kidney organoids are suitable 3D models of the kidney with various compartments that represent all cell types, and have been used in previous studies to model kidney fibrosis, the batch-to-batch variations and the presence of off-target cell types hamper standardization [4]. On the other hand, Kidney-On-A-Chip microfluidic models often only include one cell-type, namely proximal tubule cells [5–7], or combine two or more cell types of non-kidney (e.g. HUVECs [8,9]), or non-human origin (e.g. rat or mice endothelial cells or podocytes [10,11]). While no existing chip model includes multiple human kidney-derived supporting cell types to model human interstitial kidney fibrosis to the best of our knowledge. Thus, a more standardizable and scalable system is needed that allows to model complex cellular interactions that drive kidney disease. One conserved mechanism across all kidney diseases is epithelial injury, which can be caused by direct toxic or hypoxic injury to epithelial cells, or by proteinuria due to injury to the glomeruli [12]. Endothelial cells of the renal interstitium are also critical players in kidney disease and strong evidence suggests that perivascular cells (fibroblasts and pericytes) as key drivers of fibrosis [13]. Once activated, they detach from the renal microvasculature, triggering capillary loss with subsequent hypoxic tubule epithelial injury and fibrosis [14]. Despite the above mentioned recent progress in advanced *in vitro* modeling of the human kidney, including the (bioprinted) iPSC-derived kidney organoids [15], tubuloids [15,16] or (perfusable) tubules-on-a-chip [17], all of these models are difficult to standardize, and the interplay between injury to the epithelial tubular compartment and the response of the interstitial compartment is not well understood. Therefore, we aimed to create a three-dimensional *in vitro* model involving the key renal cell types (endothelium, pericytes and tubule epithelium) to investigate this crosstalk in a standardized and scalable disease model using bioprinting. We established this bioprinted model with a representative architecture; including distinguishable cellular compartments that are in close contact with each other without the need of a separating membrane in between cell types. We used highly characterized novel human cell lines to study the human interstitial fibrotic response to injury, and demonstrated the ability for high-throughput bioprinting.

2. Results

2.1. Novel human tubulo-interstitial kidney cell lines

The biofabrication of kidney interstitial space requires the use of different cell types. We propose that tubule-epithelial injury with subsequent activation of platelet-derived growth factor receptor beta (PDGFRβ$^+$) perivascular mesenchymal cells [13,18] is a key mechanism across virtually all types of kidney injury leading to CKD [12,13]. Tubule epithelial injury can, for instance, be caused by proteinuria due to leakiness of the renal filtration barrier by e.g. glomerulonephritis or diabetic nephropathy, or by direct toxic or ischemic injury to the tubule. Tubule injury has been shown to induce de-differentiation of the tubule-epithelial cells, a process termed partial epithelial-mesenchymal transition [19,20]. Dedifferentiated tubule-epithelial cells activate mesenchymal cells to detach from capillaries, driving capillary loss with subsequent fibroblast-to-myofibroblast differentiation and fibrosis [14]. In this process, immune cells, such as macrophages, are also critically involved, and we have shown that the top cellular crosstalk partners of fibrosis driving mesenchymal cells in human kidney fibrosis are indeed injured tubule-epithelial cells and immune cells [13]. However, to simplify this model, we focused on the three primarily involved resident renal cell types of the tubulo-interstitium: i) proximal tubular epithelial cells, ii) kidney endothelial cells and iii) perivascular PDGFRβ$^+$ renal mesenchymal cells.

Since currently no well characterized human kidney tubulo-interstitial cell lines are broadly available, we isolated cells from cortical wedge biopsies of human nephrectomies (Fig. 1A) to generate and characterize novel cell lines for our model. To isolate the cells, we utilized staining of the surface markers PDGFRβ (mesenchyme), CD31 (endothelium) and CD10 (proximal tubule) with subsequent cell isolation (Fig. 1B). To isolate renal interstitial PDGFRβ$^+$ mesenchymal cells, we first separated glomeruli from the cortical wedge biopsy using sieving [21], which removed mesangial PDGFRβ$^+$ cells [22], and then isolated PDGFRβ$^+$ cells by magnetic activated cell sorting (MACS). CD31$^+$ and CD10$^+$ cells were isolated similarly using MACS, while avoiding glomeruli (removal using the commonly used sieving protocols) to enrich interstitial endothelial cells or proximal tubule epithelial cells. Cells were immortalized using simultaneous retroviral SV40-large T (LT) and human telomerase (hTERT) transduction. Following immortalization, cells were genetically tagged using lentiviruses with different fluorochromes to allow for their visualization (Fig. 1C). To characterize the generated cell lines after immortalization and genetic tagging (Fig. 1D), we performed bulk RNA-sequencing, which demonstrated that the three cell types clearly showed a distinct mRNA expression profile (Fig. 1E). We next compared the transcriptome of each cell line to our published single cell RNA-sequencing (scRNA-seq) data of human kidneys [13] (Fig. 1F), confirming a proximal tubule epithelial identity of the CD10$^+$ cells, a mesenchymal identity of the PDGFRβ$^+$ cell line, and an endothelial identity of the CD31$^+$ cell line. We observed some similarities of the immortalized CD31$^+$ and PDGFRβ$^+$ cell line, which we have also reported in our human kidney scRNA-seq atlas from freshly sequenced human kidney endothelial cells, as well as mesenchyme [13]. In addition, this could be due to mesenchymal gene expression of the endothelial cells, driven by the *in vitro* conditions.

To further validate our bulk RNA-sequencing data and better characterize our newly generated cell lines, we confirmed the presence of multiple cell type specific markers, performed functional assays, and demonstrated typical morphology of the cell lines (Supplement Fig. S1A). Our CD10$^+$ cells demonstrated protein expression of epithelial specific cubilin and the proximal tubule specific marker protein CD13, also known as Aminopeptidase N (APN) (Fig. 1G). Our bulk RNA-sequencing of CD10$^+$ cells confirmed this proximal tubule nature of the cells by demonstrating the presence of CD13 expression, and the absence of markers concerning other tubule segments and podocytes (Fig. 1H). To demonstrate functionality, we evaluated the apical ATP-dependent efflux transporter P-glycoprotein (P-gp) of proximal tubule epithelial cells using the fluorescent substrate Calcein-AM, that can be blocked using the small molecule compound PSC833. Cells showed accumulation of fluorescent Calcein-AM in the presence of the P-gp inhibitor PSC833, indicating functional P-gp (Fig. 1I). The CD31$^+$ cell line showed protein expression of the endothelial marker protein von Willebrand Factor (vWF) (Fig. 1J), confirming its endothelial nature.

In summary, we have generated three novel human kidney cell lines that maintained their endothelial, proximal tubular epithelial and mesenchymal expression profile after immortalization and are thus representing novel and useful tools to understand cellular and molecular mechanisms of these key resident tubulo-interstitial cell types *in vitro*.

2.2. PDGFRβ$^+$ mesenchymal cells are myofibroblast precursors and possess three-lineage differentiation capacity

To validate that PDGFRβ is indeed the right surface marker to isolate myofibroblasts and their precursors as the cellular source of kidney

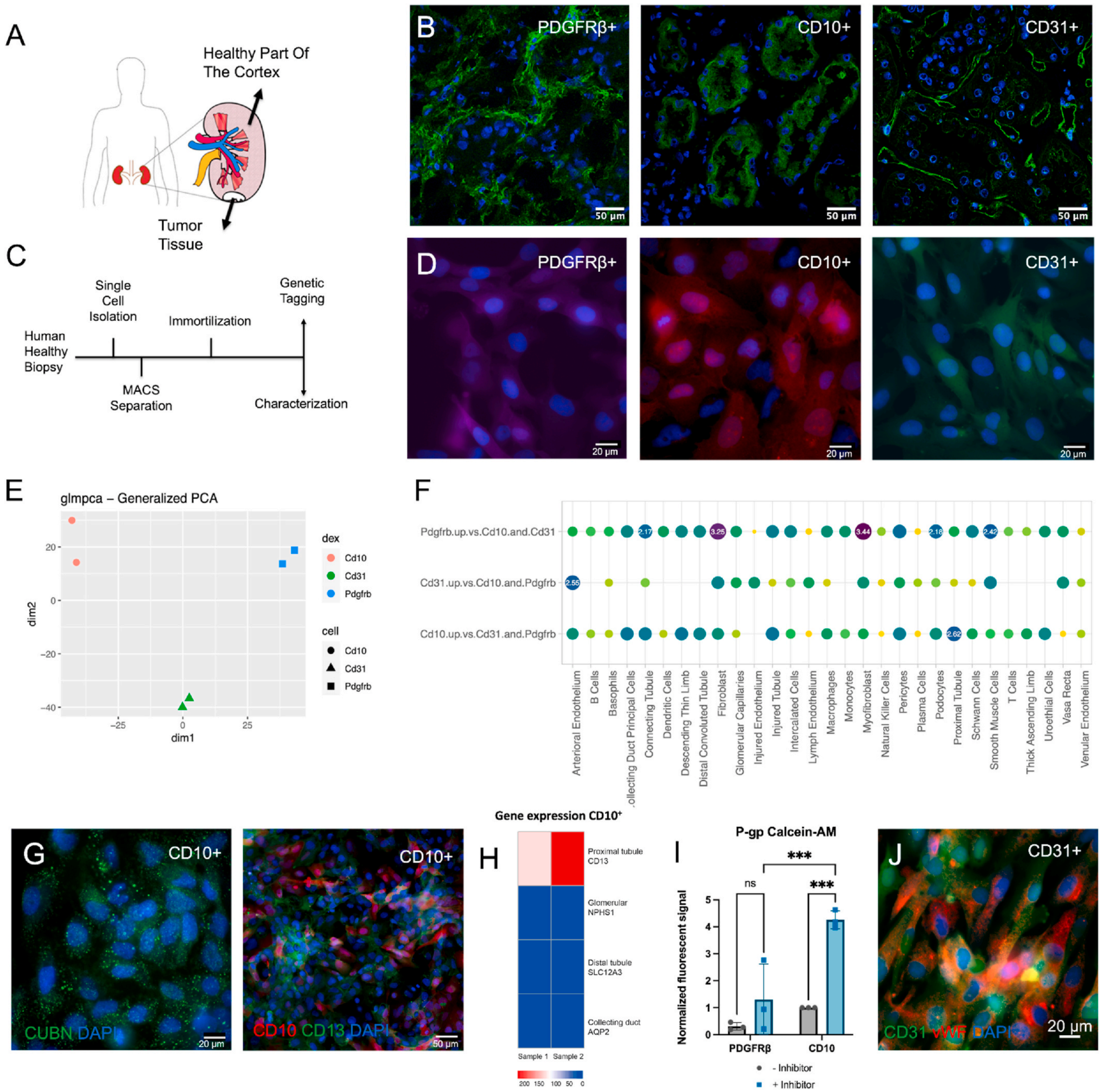

Fig. 1. Generation of stable human kidney cell lines with proven origin. A: Schematic of the human kidney and the cortex illustrates the source of isolated cells. B: Immunofluorescence staining of PDGFRβ$^+$, CD10$^+$ and CD31$^+$ specific antibodies for cells in cortex of human kidney. C: Enumeration of the workflow from isolating the cells to the generation of genetically tagged cells. D: Representative pictures of genetically labeled immortalized PDGFRβ$^+$, proximal tubular epithelial and endothelial cell lines. 4′,6-diamidino-2-phenylindole (DAPI) was used for nuclear staining. E: Principal component analysis (PCA) plot of the generated three cell lines. The three cell lines show higher variability from each other, while technical replicates are similar to each other. F: Shared DE genes between isolated cell lines and human bulk RNA seq [13]. G: CD10$^+$ (red) cells stained for cell-specific proximal tubule epithelial markers cubilin (green, left) and CD13 (green, right) including DAPI. H: Heatmap of bulk RNA-sequencing data demonstrating the genes expressed in CD10$^+$. I: P-gp Calcein-AM transporter assay of CD10$^+$ and negative control PDGFRβ$^+$ cells, with or without transporter inhibitor PSC833. ***$p < 0.001$ (one-way ANOVA analysis followed by Tukey post-test), n = 3 with each 12 replicates. J: Presence of intracellular vWF (red) in CD31$^+$ (green) cells including DAPI. (For interpretation of the references to color in this figure legend, the reader is referred to the Web version of this article.)

fibrosis, we performed a co-staining and quantification for the myofibroblast marker alpha-smooth muscle actin (α-SMA)/ACTA2 and PDGFRβ (Fig. 2A). We quantified interstitial cells in kidney sections of seven patients (excluding glomeruli and arteries/arterioles) with different levels of fibrosis (Fig. 2B). Independent of the severity of interstitial fibrosis, the vast majority of α-SMA expressing cells co-expressed PDGFRβ (Fig. 2C and D). These findings indicate that regardless of fibrosis severity, PDGFRβ is expressed by the vast majority of myofibroblasts, thus confirming our choice of surface marker for cell isolation. Of note, our recent human kidney scRNA-seq data and genetic fate tracing data in mice also confirms that virtually all myofibroblasts are PDGFRβ lineage derived [13].

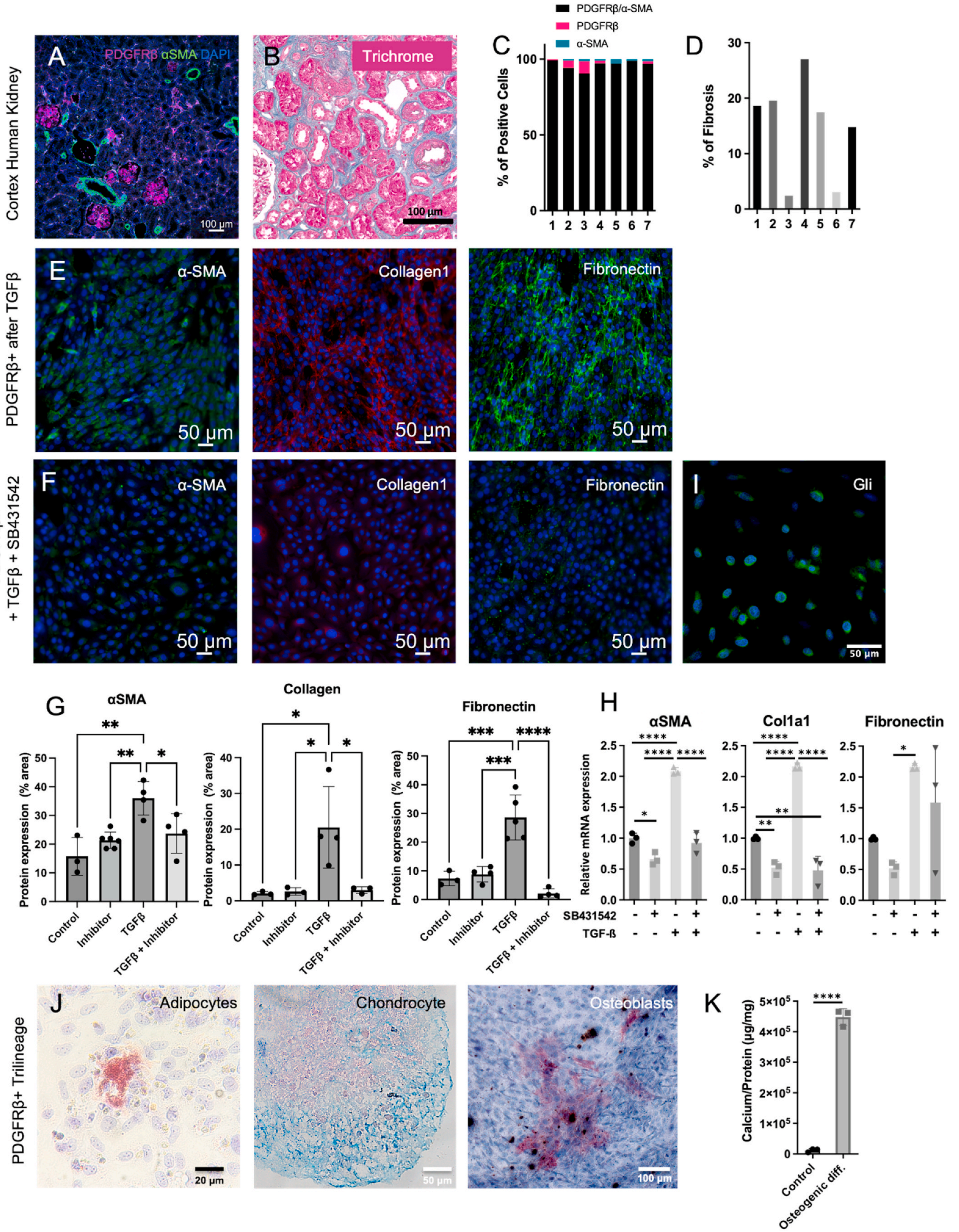

(caption on next page)

Fig. 2. PDGFRβ is the cell surface marker of myofibroblasts precursor. A: Representative immunofluorescence stainings visualizing PDGFRβ$^+$ (purple), α-SMA$^+$ cells (green) and colocalization (white) in cortex of human kidney. B: Interstitial fibrosis with collagen fibers in blue after Masson's trichrome staining of the kidney cortex derived from patients. C: Quantification of presence and colocalization of PDGFRβ and α-SMA in human patients. D: Percentage of kidney slides indicating interstitial fibrosis as quantified via Masson's trichrome staining. E: Representative immunofluorescent images of PDGFRβ$^+$ cells after TGFβ exposure, stained for α-SMA (green), Collagen1 (red) and Fibronectin (green). F: Representative immunofluorescent images of PDGFRβ$^+$ cells after TGFβ treatment in the presence of the TGFβ-inhibitor SB431542, stained for α-SMA (green), Collagen1 (red) and Fibronectin (green). G: Protein quantification of α-SMA, Collagen1 and Fibronectin in TGFβ treated and untreated PDGFRβ$^+$cells in the presence or absence of the TGFβ-inhibitor SB431542. $^*p < 0.05$, $^{**}p < 0.01$, $^{***}p < 0.001$, $^{****}p < 0.0001$ (one-way ANOVA analysis followed by Tukey post-test). H: mRNA expression in PDGFRβ$^+$ cells of α-SMA, Col1a1 and Fibronectin after 24 h of TGFβ treatment either with or without TGFβ-inhibitor SB431542. $^*p < 0.05$, $^{**}p < 0.01$, $^{****}p < 0.0001$ (one-way ANOVA analysis followed by Tukey post-test). I: Gli expression (green) with DAPI (blue) in PDGFRβ$^+$ cell line. J: Representative images of adipocytes by Oilred O + hematoxylin, chondrocytes by Alcian blue and osteoblasts by alkaline phosphatase + von Kossa + hematoxylin staining on PDGFRβ$^+$ cells after *in vitro* differentiation into respective cell type. K: Calcium protein measurement of osteoblasts formed by PDGFRβ$^+$ cells after differentiation. $^{****}p < 0.0001$ (unpaired *t*-test). (For interpretation of the references to color in this figure legend, the reader is referred to the Web version of this article.)

We next sought to verify that the novel PDGFRβ$^+$ cell line indeed represents a suitable tool to study myofibroblast differentiation and activation. The addition of transforming growth factor β (TGFβ), the hallmark growth-factor involved in myofibroblast differentiation and activation, resulted in increased α-SMA, collagen1a1 (Col1a1) and fibronectin (FN) expression on protein as well as gene level (Fig. 2E, Supplement Fig. S1B), confirming myofibroblast differentiation and activation. Exposure of the cells to TGFβ inhibitor SB431542 significantly abolished this process, as shown on both protein and gene level (Fig. 2F–H, Supplement Fig. S1C). Interestingly, inhibition of TGFβ signaling by SB431542 was further able to reduce α-SMA and Col1a1 gene expression even in the absence of TGFβ, pointing towards activity of this pathway in the isolated cell line, independent of external stimulation (Fig. 2H).

We have previously demonstrated that a subpopulation of perivascular PDGFRβ$^+$ cells, defined by expression of Gli1, are the major source of renal myofibroblasts [18,23] and are mesenchymal stem cell-like cells of the kidney. Immunostaining for Gli1 demonstrated that the novel PDGFRβ$^+$ cell line shows strong expression of this zinc finger transcription factor (Fig. 2I). We further demonstrated that the PDGFRβ$^+$ cell line possesses tri-lineage differentiation capacity towards osteoblasts, adipocytes and chondrocytes (Fig. 2J), and demonstrated increased calcium from PDGFRβ$^+$ cell lysates after osteogenic differentiation (Fig. 2K). Taken together, these findings confirm that the generated PDGFRβ$^+$ cell line has conserved key features of Gli1$^+$ MSC-like cells and represents a novel tool to study renal myofibroblast differentiation and activation *ex vivo*.

2.3. Dissecting mechanisms of myofibroblast differentiation ex vivo

As this novel PDGFRβ$^+$ cell line represents a unique tool to study myofibroblast differentiation and activation *ex vivo*, we next wanted to dissect the key molecular pathways involved in this process. As the TGFβ pathway in particular is fundamental to the phenotypic transition between fibroblasts to myofibroblasts [24], we stimulated the PDGFRβ$^+$ cell line with TGFβ for 24 or 72 h as compared to non-stimulated cells, followed by bulk RNA-sequencing (Supplement Fig. S1D-F, S2). Principal component analysis (PCA) revealed three distinct clusters divided by treatment (Fig. 3A), demonstrating the activating effect of TGFβ treatment for PDGFRβ$^+$ cells towards myofibroblasts. After 72 h, we observed upregulation of many genes that have been reported to be involved in human kidney fibrosis, including *FOXS1*, *TNFSF15*, *LINC0711*, *SERPINE2*, *FZD8*, *EGR2*, *MMP-2* and *KIF26b* (Fig. 3B). Most importantly, we found signature myofibroblast gene periostin (*POSTN)* and fibronectin type III domain containing 1 (*FNDC1*) to be strongly upregulated. *POSTN* is a key myofibroblast gene [13] is found to be strongly induced in renal fibrosis of animal models, whereas deletion of *POSTN* in animal models attenuated renal fibrosis [25–28]. In the same manner, *FNDC1* has been described to be associated with the induction of the myofibroblastic phenotype [29,30]. To validate some of these findings on protein level, we performed immunostaining of the myofibroblast markers periostin (POSTN) and fibronectin (FNDC1) 72 h after TGFβ exposure and observed an increase in both (Fig. 3C). Early after TGFβ treatment, the PDGFRβ$^+$ cell line showed an increase of profibrotic genes, such as *IL11* and *EDN1*. At the same time, (myo)fibroblast marker genes, such as *ACTG2* [31] and *IGFBP3*, which is described as a key mediator of tubulointerstitial fibrosis [32], were upregulated (Fig. 3B). While later at 72 h, we observed upregulation of *GDF15*, which is described as a kidney protective factor after injury [33], and *MMP-2,* an activator of TGFβ that is implicated in the initiation of kidney fibrosis [34,35]. The upregulation of these key genes at 24 h and 72 h demonstrated that the PDGFRβ$^+$ cells can be used to model fibroblast-to-myofibroblast transition after TGFβ stimulation *in vitro*.

To further understand the gene expression patterns, PROGENy, a resource that uses publicly available signaling perturbation experiments to generate common gene pathways and their activities, and doRothEA, a tool that looks into transcription factors and their target gene interactions, were employed. PROGENy analysis predicted increased activity of PI3K signaling early after TGFβ stimulation (24 h) (Fig. 3D). Strong evidence indicates that PI3K plays a major role in pericyte to myofibroblast differentiation [36]. Other signaling pathways that play a role in kidney fibrosis include the protective response of estrogen related pathways [37,38], whereas an aggravating fibrotic response is visible in hypoxic signaling [39,40]. A late response after TGFβ stimulation includes renal fibrosis related pathways, such as NFKb [41], Wnt [42], p53 [43] and MAPK [44] signaling (Fig. 3D). Taken together, the PROGENY analysis indicates increased activity of PI3K, NFKb, Wnt, p53 and MAPK signaling, however, we have not validated this data on proteome level.

Transcription factor (TF) activity prediction based on TF regulons (DoRothEA) showed increased TF activity of E2F1 and E2F4 at 24 h after TGFβ stimulation, while TCF12, TEAD1 and TP53 showed a continuously increased estimated activity at 72 h (Fig. 3E). E2F transcription factors are essential in cell cycle regulation but are also described to affect senescence and fibrosis [45]. TEAD1 has recently been identified as a key player in cardiac pro-fibrotic fibroblasts activation [46], and was found to be highly associated with extracellular matrix (ECM) expression across fibroblast cell types [47]. The YAP/TAZ pathway, in which TEAD1 plays a role, has also been described to regulate renal fibrosis [48], demonstrating that PDGFRβ$^+$ cells upregulate critical pathways for kidney fibrosis. In line with this, gene set enrichment analysis revealed upregulation in pathways associated with ECM production and organization (Fig. 3F).

In summary, this data indicated that TGFβ stimulation of the newly generated PDGFRβ$^+$ cells resembles various aspects of fibroblasts to myofibroblast differentiation in the human kidney and thus the novel cell line represents a suitable model to study human kidney fibrosis in the dish.

2.4. Bioprinting of a kidney tubulo-interstitial structure

Accurate modeling of a 3D kidney tubulo-interstitium requires the dispersion of multiple types of cells into predefined spatially controlled areas, which can be achieved by the use of a bioprinter. When designing a 3D model, the technical and biological limitations, including the

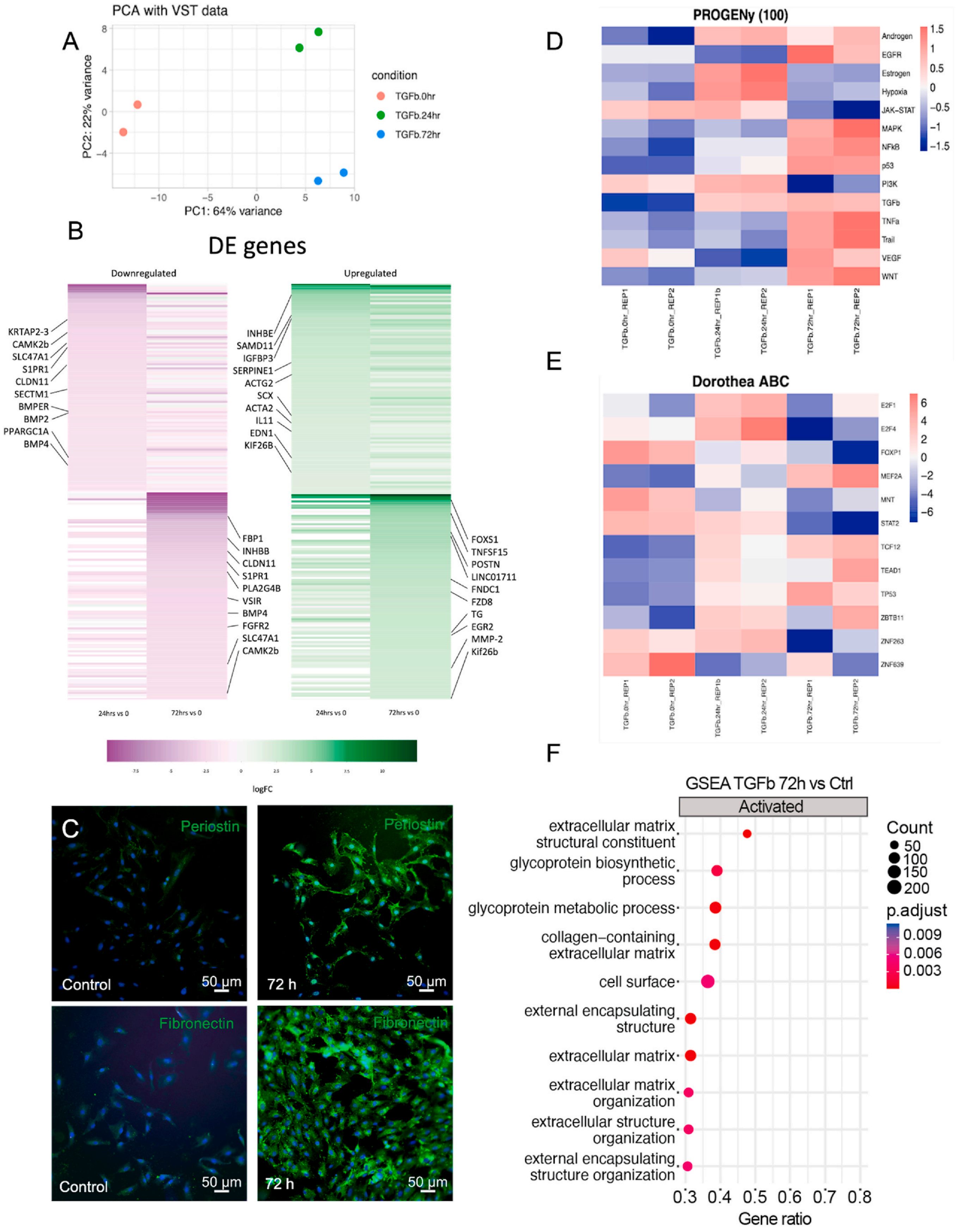

(caption on next page)

Fig. 3. Time course of PDGFRβ$^+$ cells treatment with TGFβ represents fibroblast-to-myofibroblast differentiation. A: principal component analysis (PCA) of treated and untreated cells. B: Selected differentially expressed (DE) up- and down regulated genes in PDGFRβ$^+$ cells exposed to either 24 h or 72 h of TGFβ compared to control, full figure in Supplement Fig. S3. C: Representative immunofluorescence images of TGFβ treated PDGFRβ$^+$ cells stained for periostin (green) and fibronectin (green) with DAPI (blue) 72 h post exposure. D: Pathway analysis based on pathway responsive genes using PROGENy, color indicating the predicted activity per pathway. E: Transcription factor (TF) activity prediction based on TG regulons (DoROthEA), color indicating relative predicted activity per TF. F: GO-term enrichment analysis of differentially expressed genes using DEseq 2 analysis. (For interpretation of the references to color in this figure legend, the reader is referred to the Web version of this article.)

resolution of the printer and the duration of the printing process, should be considered. Three different types of bioprinters are available, including inkjet, laser-assisted and extrusion-based [49]. We here utilized extrusion-based bioprinting, which has the advantages of being applicable to a wide range of bioinks from medium to high viscosity with high cell viability due to low the shear stress applied on cells during the printing process. Furthermore, this process is fast, and allows the printing of large, relevant constructs with pre-defined complex architectures [50]. We here utilized a 3DDiscovery (regenHU) bioprinter equipped with two temperature-controlled volumetric printheads for extrusion bioprinting. A relevant 3D model using a simple fibrinogen/gelatin-based hydrogel as bioink was designed (Fig. 4A). The goal was to print tubule-like structures (Fig. 4B, blue circles) of CD10$^+$ cells surrounded by an interstitium of PDGFRβ$^+$ and CD31$^+$ cells (Fig. 4B, pink structure) according to a predefined architecture. The 3D model was generated with computer-aided design (CAD), converted to stereolithography (STL), and sliced with the integrated BioCAM slicer to generate a G-code for the printing of a 14 × 14 mm construct directly in a 12-well plate (Fig. 4C).

In this study, we used a mixture of 7.5 % gelatin and 5 mg/mL fibrinogen as a natural bioink for encapsulating living cells during printing. Gelatin is produced by denaturation of the triple-helix structure of collagen into single-stranded molecules [51]. It is less immunogenic compared to collagen, and still contains the Arg-Gly-Asp (RGD) sequence, which contributes to cell adhesion, differentiation, and proliferation [51,52]. The other component of the bioink, fibrinogen, is also biocompatible, biodegradable, non-immunogenic, and is able to induce cell attachment, proliferation, and ECM formation [49,53]. Mixing of the highly viscous gelatin with the fluidic fibrinogen prevents the collapse of the deposited cell loaded material and maintains the 3D structure of the constructs both during and after the printing. Immediately following printing, fibrinogen is crosslinked using thrombin; one of the main components in blood-clotting [54]. It mediates the cleavage of fibrinopeptides and initiates the lateral aggregation of protofibrils and fibrin formation, leading to a structural fibrin network contributing to gel shaping [54,55]. A SEM image of cell-free printed fibrinogen/gelatin bioink after crosslinking depicts the endogenous microstructure and the network of this mixed hydrogel (Fig. 4D).

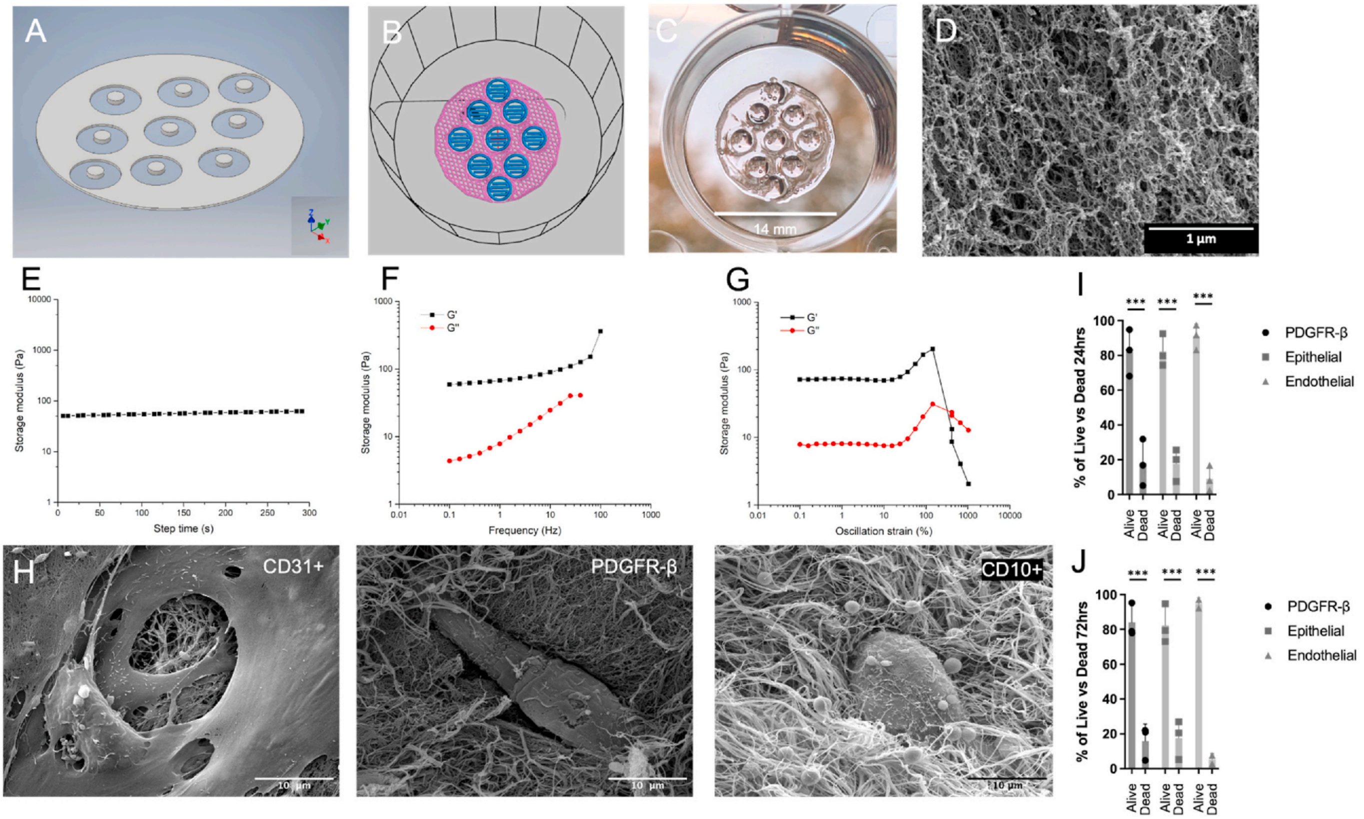

Fig. 4. Description of the 3D-bioprinting model. A: A computer-aided design as a template for printing a heterogeneous tissue construct composed of two tissue parts in a 12-well plate. B: The bioink containing CD10$^+$ cells for the tubule-like structure was assigned to the small inserts within the constructs (blue) and the bioink containing CD31$^+$ and PDGFRβ$^+$ cells for the interstitium was assigned to the surrounding matrix (pink). C: 3D printed and crosslinked fibrinogen-gelatin structure containing no cells. D: Environmental scanning electron microscopic (ESEM) - picture demonstrates the microstructure of fibrinogen-gelatin mixture without cells after 3D printing. E, F, G: Viscoelastic behavior measured by storage modulus, varying time, frequency, or oscillation strain with dynamic storage modulus (G′) in black and loss modulus (G”) in red. H: ESEM picture of cell lines as printed into the fibrinogen-gelatin mix. I–J: Percentages of live and dead cells 24 h and 72 h after printing. $^{***}p < 0.001$, (one-way ANOVA analysis followed by Tukey post-test). (For interpretation of the references to color in this figure legend, the reader is referred to the Web version of this article.)

To characterize the rheological properties of our bioink, we next performed a time-sweep test at a constant strain of 0.5 % and frequency of 1 Hz. During the measurement (5 min), the storage modulus has shown a constant profile, demonstrating the unchanged internal structure of the hydrogel. This is due to the fact that measurements were always performed after complete crosslinking. The measurements of the hydrogel indicate a very soft gel with a storage modulus of 73 ± 11 Pa. (Fig. 4E). To obtain the viscoelasticity behavior and strength of the hydrogel, both frequency and amplitude sweep tests were performed, respectively. The frequency-sweep data was recorded at different frequencies in the range of 0.1–100 Hz at a constant oscillation strain of 0.5 %, resulting in the dynamic storage (G′) and loss modulus (G″) of the material. The information about the solid-like (elastic) behavior of the material is given by G′, while G″ gives information about the liquid-like (viscous) behavior. Fig. 4F demonstrates the logarithmic plot of modulus, indicating that the material is a gel within this regime by showing higher values of G′ compared to G″ at all frequencies (Fig. 4F). The slight decrease of the storage modulus for lower frequencies suggests that the hydrogel is not purely elastic, which is expected for protein-based hydrogels. An amplitude-sweep test was performed at 1 Hz and 25 °C. The examination of storage and loss data at the fixed frequency demonstrates that at larger strains above 300 %, G" exceeds G', indicating rupture of the hydrogel. Above 40 %, an increase in moduli is observed before breakage. This may be due to some stiffening by extensional strain on the nanofibrillar structures. Below 40 %, a broad linear viscoelastic regime (LVR), in which the modulus is independent of strain, is observed. This shows that at these low amplitudes, the internal structure of the hydrogels is maintained without any noticeable changes (Fig. 4G).

Upon bioprinting the cell lines separately, all three cell lines showed a good embedding into the bioink micro-structure (Fig. 4H, Supplement Fig. S4B) and quantification of live/dead stained bioprinted cells within the bioink at 24 h and 72 h indicated a good overall survival rate for all three cell lines (Fig. 4I and J, Supplement Fig. S4C, D). Next, we moved towards the bioprinting of all three cell types together. The cells were bioprinting according to a predefined architecture, with inserts containing $CD10^+$ epithelial cells, surrounded by a matrix containing $PDGFR\beta^+$ and $CD31^+$ cells to recapitulate the biologically relevant tubule and interstitium architectures at 0 and 7 days after printing (Fig. 5A).

2.5. *Modeling of fibrosis in the bioprinted human kidney tubulo-interstitium*

TGFβ is the known master regulator of fibrosis [56,57] and we have demonstrated that TGFβ treatment resulted in fibroblast-to-myofibroblast transition of the generated $PDGFR\beta^+$ cell line. Thus, to model kidney fibrosis within this 3D bioprinted tubulo-interstitial model system, we starved the bioprinted constructs for 8 h (0.5 % FCS) at day 4 after printing with subsequent TGFβ stimulation for 24 h, followed by qPCR analysis and immunostaining at day 7 (Fig. 5B). TGFβ treatment resulted in increased collagen 1 expression on protein level as well as a trend towards increased collagen 1 mRNA expression ($p = 0.09$) (Fig. 5C and D, respectively). While the spatially defined compartments were still distinguishable in the TGFβ treated constructs, the tubular compartment started to show less defined borders, with $CD10^+$ cells embedded in the ECM. A possible explanation for the only slightly elevated mRNA levels of Col1a1 could be that the time point of harvest was not ideal for peak mRNA expression measurement, however, the significantly increased protein indicates the development of fibrosis in this model. In addition, protein quantification of αSMA, a marker of activated myofibroblastic cells, showed a significant increase that further demonstrates the transition of fibroblasts to myofibroblasts in our injured bioprinted construct (Fig. 5E).

As mentioned above, one conserved mechanism of kidney fibrosis across virtually all kidney diseases is tubule epithelial injury. Tubule epithelial injury can be caused by proteinuria due to leakiness of the glomerular filter in e.g. diabetes or glomerulonephritis, or by hypoxic or toxic injury to the epithelial cells. Injured tubule-epithelial cells dedifferentiate and flatten, and mediate fibrosis by direct crosstalk to mesenchymal cells with subsequent myofibroblast differentiation. Thus, to model this common cellular crosstalk mechanism driving kidney fibrosis, we tested a second disease model with toxic injury of tubule epithelial cells by nephrotoxic ochratoxin (OTA) to injure specifically $CD10^+$ epithelial cells alone prior to bioprinting. OTA primarily targets the kidney by accumulating in proximal tubule epithelial cells, where it promotes DNA methylation, pyroptosis and apoptosis, leading to renal fibrosis [58].

$CD10^+$ cells were treated with OTA for 16 h as compared to vehicle (DMSO) treated $CD10^+$ cells (Supplement Fig. S5A-C). 24 h after injury, the $CD10^+$ cells were 3D bioprinted into one compartment surrounded by $PDGFR\beta^+$ and $CD31^+$ cells in a second compartment as described earlier. Interestingly, this experiment resulted in increased Col1a1 expression on mRNA level of the whole construct, while only $CD10^+$ were exposed to the toxin prior to the bioprinting (Fig. 5F). This is suggesting a mechanism of cellular crosstalk of injured epithelial cells to fibroblasts with subsequent fibroblast activation and transition towards myofibroblasts.

To utilize this novel model system for screening approaches to identify novel interventional strategies for human kidney fibrosis, the system needs to be scalable towards multi-well plates. To demonstrate that our system is indeed scalable, we adapted the 3D design previously mentioned, to fit into 96-well plates (Fig. 5G). A disk representing the tubular-like structure was printed (blue, Fig. 5G), followed by the interstitium-like structure (pink, Fig. 5G), as two concentric disks of 1.7 mm and 5 mm diameter, respectively. The G-code was adapted to print multiple constructs in a row with a printing time of less than 2 min per construct. Directly after printing, we demonstrated that the predefined spatially controlled compartments are present at 96-well level as well (Fig. 5H).

Representative immunofluorescence images at day 7 after printing of the constructs within the 96-well plate indicated the presence of the same compartments of $CD10^+$ cells (red), surrounded by $CD31^+$ (green) and $PDGFR\beta^+$ cells (Fig. 5I and L), confirming that the described system is scalable and can be utilized for screening in multi-well plates. In addition, we demonstrated injury modelling to be feasible in the 96-well format (Fig. 5J), as shown by ECM remodeling after TGFβ (left) and OTA treatment (right). After exposure of the micro constructs to TGFβ, or pre-exposure of only $CD10^+$ to OTA prior to printing, an increase of Col1a1 on a protein level was observed (Fig. 5K and L, Supplement Fig. S5D). After TGFβ treatment, collagen deposition in the bioprinted constructs was most prominent in the interstitial compartment, while after pre-exposure of $CD10^+$ cells to OTA, most collagen was observed in the tubular compartment (Fig. 5J).

To further demonstrate that the cellular crosstalk between the tubular epithelial and interstitial compartment drives fibrosis, constructs containing a) all three cell types, b) only $PDGFR\beta^+$ and $CD31^+$ cells, or c) OTA pre-exposed $CD10^+$ cells in the tubular compartment without the interstitial compartment, were printed. Bioprinted constructs were treated with supernatant of OTA-injured $CD10^+$ cells, resulting in a rearrangement of the architecture and upregulation of collagen 1 on a protein level, both in the a) three cell type and b) interstitium-only constructs (Supplement Fig. S6A-F). The constructs containing only injured $CD10^+$ cells did not show any collagen 1 deposition (Supplement Fig. S6G). Further investigation of the supernatant with a human cytokine array revealed upregulation of various inflammatory cytokines including IL6, IL8, Osteopontin, TIMP-1 and 2 (Supplement Fig. S6H), that are known to drive fibrosis [59–62]. Taken together, this data indicates that paracrine signaling from epithelial cells to interstitial fibroblasts is required to drive fibrosis and extracellular matrix remodeling of the bioprinted construct.

Overall, these experiments indicate that our bioprinted tubule-

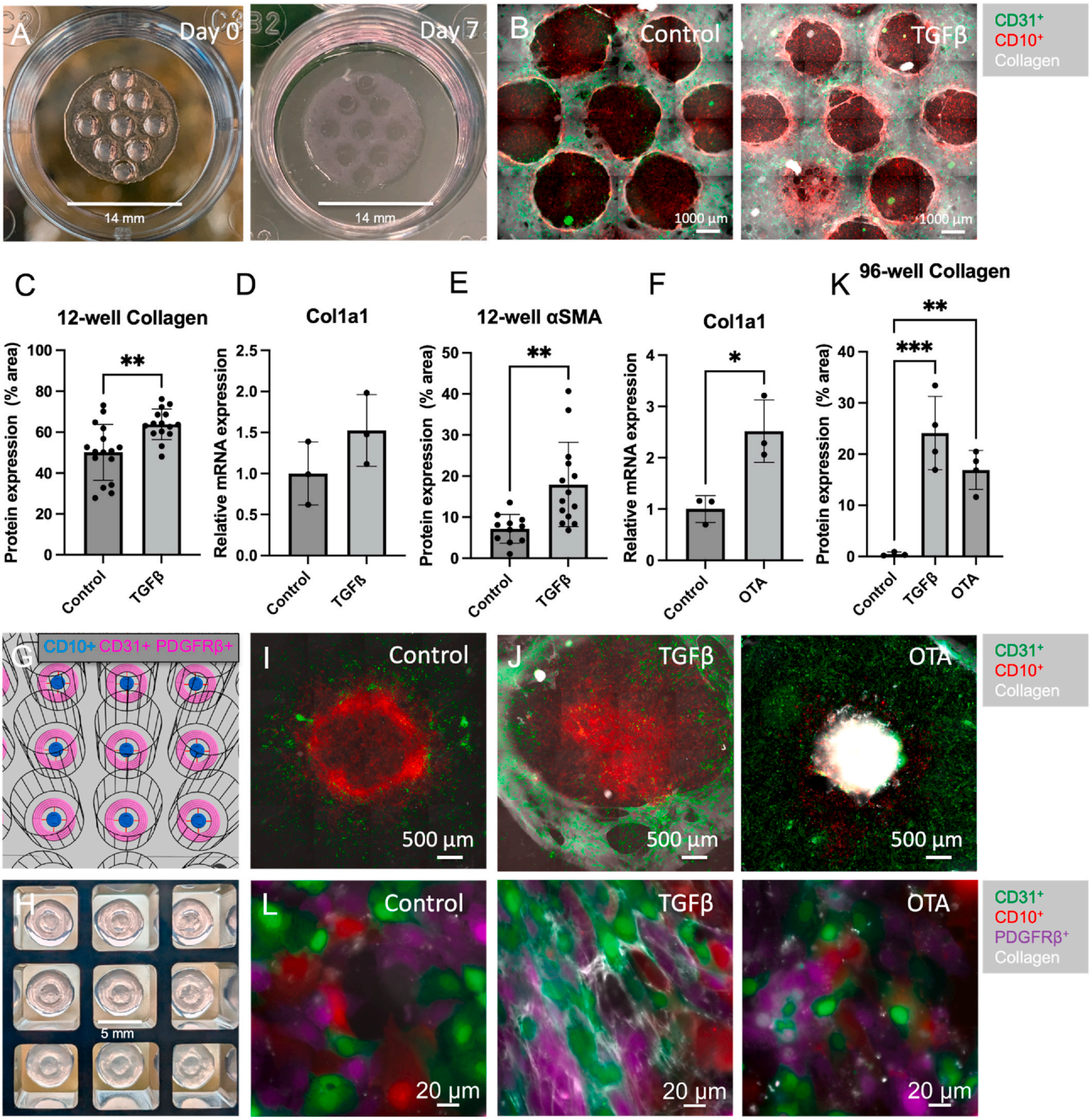

Fig. 5. Modeling fibrosis in the bioprinted construct. A: Bioprinted construct in 12-well format, containing all three cell lines before crosslinking at day 0 (left) and after crosslinking at day 7 (right). B: Representative immunofluorescence images of the untreated control bioprinted construct (left), and TGFβ-treated construct (right) on day 7 after printing, with a clear separation between tubule compartment of CD10$^+$ cells (red) and stromal compartment with CD31$^+$ cells (green) and PDGFRβ$^+$ (not shown). Collagen is depicted in white. C: Protein quantification based on positive area percentage for collagen for Control and TGFβ-treated in the 12-well constructs. $^{**}p < 0.01$ (unpaired *t*-test). D: mRNA expression of Col1a1 in bioprinted constructs after 24 h of TGFβ exposure, $p = 0.09$ (unpaired *t*-test). E: Protein quantification of αSMA in untreated or TGFβ treated bioprinted 12-well constructs, data depicted as percentage of area positive for αSMA. $^{**}p < 0.01$ (unpaired *t*-test). F: mRNA levels of Col1a1 in 12-well untreated control or OTA treated constructs. $^{*}p < 0.05$ (unpaired *t*-test). G: Template for printing a simplified heterogeneous tissue construct composed of two tissue parts in a 96-well plate, with a tubular compartment containing CD10$^+$ (blue), and an interstitium containing CD31$^+$ and PDGFRβ$^+$ cells (pink). H: Mini constructs containing all three cell types directly after printing at day 0, demonstrating distinguishable compartments. I: Overview of the mini constructs containing all cell types at day 7 after printing in the 96-well format for untreated control. J: Representative immunofluorescence images of TGFβ- or OTA-treated mini constructs. The center is composed of CD10$^+$ cells (red), surrounded by CD31$^+$ cells (green) and PDGFRβ$^+$ (not shown), and collagen in white. K: Collagen quantification in 96-well format for untreated control, TGFβ and OTA, expressed as the percentage of total area above a threshold. $^{**}p < 0.01$, $^{****}p < 0.001$ (one-way ANOVA analysis followed by Tukey post-test). L: Representative immunofluorescence images showing CD10$^+$ cells (red), surrounded by CD31$^+$ cells (green) and PDGFRβ$^+$ (purple) for control, TGFβ- or OTA-treated 96-well mini constructs. Collagen fibers are seen in white (63× magnification). (For interpretation of the references to color in this figure legend, the reader is referred to the Web version of this article.)

interstitium as full size and in 96-well format responds well to pro-fibrotic stimuli comparable to pro-fibrotic processes in the human kidney during kidney fibrosis development. We demonstrated a fibrotic response of PDGFRβ$^+$ mesenchymal cells by i) a direct activation of mesenchymal cells via TGFβ, as well as by ii) a separate toxic injury to tubule-epithelial cells prior to bioprinting and addition of CD31$^+$ and PDGFRβ$^+$ cells. The latter strongly confirms the important role of tubule-interstitial crosstalk with injured epithelial cells activating mesenchymal cells, even if the different cell types are printed in different compartments.

3. Discussion

Kidney function inversely correlates with interstitial kidney fibrosis, hence, the development of novel targeted anti-fibrotic therapies that could be added to current gold-standard therapies holds promise to provide a new therapy for CKD and stabilize kidney functional decline. For the development of anti-fibrotic therapies, accurate high-throughput *in vitro* platforms are needed for validation purposes and compound screenings. Here, we established a scalable bioprinted three-dimensional kidney tubulo-interstitium that allows us to model human kidney fibrosis *in vitro*. To this end, we isolated, immortalized and characterized three kidney biopsy-derived cell lines. In addition, we confirmed the identity of each cell line, most specifically PDGFRβ$^+$ cells to verify its myofibroblast lineage. In this model system, direct activation of fibroblasts by TGFβ or tubule epithelial specific injury by OTA resulted in fibrosis.

Accumulating evidence has demonstrated that tubule epithelial cells are not only targets of injury but also have a driving role towards interstitial inflammation and fibrosis. This is observed when incomplete repair of injured tubular epithelial cells leads to the progression of acute kidney injury (AKI) to CKD [63–65]. Using scRNA-sequencing, we have demonstrated that injured epithelial cells in human kidneys are among the top crosstalk partners of fibrosis driving mesenchymal cells [13]. We here demonstrate in a bioprinted 3D kidney tubule-interstitium model that cell-specific injury of human tubule epithelial cells (OTA injury prior to printing) drives fibroblast activation and collagen expression causing fibrosis. Thus, representing an *ex vivo* model of tubule-interstitial crosstalk driving kidney fibrosis.

Besides epithelial cells, microcapillaries and endothelial cells also play a major role in kidney fibrosis. Endothelial cell injury and death consequently leads to pericyte detachment, resulting in peritubular capillary rarefaction and tissue hypoxia, driving tubulointerstitial fibrosis [66,67]. In this study, we isolated, immortalized and tagged epithelial cells, endothelial cells and PDGFRβ$^+$ fibroblasts from human kidney tissue. We compared their transcriptional profile to human kidney scRNA-seq data [13,67], confirming the mesenchymal, endothelial and epithelial cell identity, despite immortalization and *ex vivo* artifacts caused by tissue culture and plastic exposure. Of note, the similarity between the endothelial cells and mesenchymal cells is likely caused by an expression of mesenchymal genes due to endothelial cell injury driven by the *in vitro* conditions, but were also observed in our human kidney scRNA-seq atlas from freshly sequenced human kidney endothelial cells [13,67]. The bulkRNA seq of PDGFRβ$^+$ cells after injury stimuli revealed upregulation of genes involved in myofibroblast differentiation, such as *FOXS1* and *SH3RF3*, indicating that these cells are an accurate representation of the human situation. Of note, immune cells are certainly also of key importance in driving fibrosis but were not included in this study. This is a current limitation of the model. One of the strengths of this study includes the 3D nature of the model using a co-culture of three novel and well-characterized immortalized cell lines. Besides being more physiological due to network formation in a non-monolayer fashion, close cellular -contact and -communication [68], the 3D printed compartmentalization also allows us to study the effects of cell type-specific injury to fibrosis, instead of stimulating all cell types simultaneously. It has also been shown that a 3D microenvironment allows for a more sensitive response to nephrotoxic stimuli, and could provide a better predictive model for drug toxicity compared to 2D models [69,70]. Moreover, our bioprinted model is fully automated, user-independent and reproducible, cost-effective and fast, with an estimated 1,33 euros per bioprinted construct that can be printed in 1–2 min. From the high-throughput perspective, we can obtain a multitude of read-outs, such as gene- and protein expression within the 96-well plate, and no additional pumps or software-guided platforms are required to sustain the constructs after printing.

We believe that this model, particularly with the novel, well characterized, genetically tagged cell lines represents a scalable testing system for genetic or pharmacologic perturbation and thus can help in preclinical screening experiments.

4. Material and methods

4.1. Ethics

The local ethics committee of the University Hospital RWTH Aachen approved all human tissue protocols (EK-016/17). Kidney tissue was collected from the Urology Department of the Hospital Eschweiler from patients undergoing (partial) nephrectomy. All patients provided informed consent, and the study was performed in accordance with the Declaration of Helsinki.

4.2. Human tissue processing and single cell suspension

Generation of single cell suspension was performed in the cell culture laboratory under sterile conditions. Kidney tissues were transferred into DMEM medium (Gibco 31885) containing 1 % penicillin/streptomycin and were separated from the capsules. The tissue was sliced into approximately 0.5–1 mm^3 pieces and were mashed. In order to remove glomeruli, the small kidney fragments were gently sieved through the 100 μM strainer. The preparation was rinsed repeatedly with DMEM-Medium, and the obtained suspension was passed through a 70 μm strainer. The final suspension was centrifuged for 5 min at 300×*g* at 4 °C and the pellet was resuspended in DMEM medium. Cell density was determined by counting using a Neubauer chamber.

4.3. Generation of human kidney -PDGFRβ$^+$, -endothelial and tubular epithelial cell lines

All cells were isolated from a healthy part of the human kidney cortex of a nephrectomy specimen: PDGFRβ$^+$ cells were derived from a 71 years old male patient, CD31$^+$ cells from a 40 years old male patient, and CD10$^+$ cells from a 55 years old male patient. To isolate these cell types, a single cell suspension was generated (as described above) from each sample, followed by MACS separation (Miltenyi biotec, autoMACS Pro Separator, # 130-092-545, autoMACS Columns #130-021-101). For the isolation of PDGFRβ$^+$ cells, the cell suspension was stained in two steps using first a specific PDGFRβ antibody (R&D # MAB1263 antibody, dilution 1:100) followed by a second incubation step with an Anti-Mouse IgG1-MicroBeads solution (Miltenyi, #130-047-102). Following MACS, cells were cultured in DMEM media (Thermo Fisher # 31885) enriched with 5 % FCS and 1 % Penicillin/Streptomycin for 14 days. In order to isolate endothelial cells, the prepared cell suspension sample was incubated with CD31-Microbeads (Miltenyi biotec # 130-091-935) and proceeded to magnetic separation, subsequently. Afterwards, endothelial cells were maintained in EGM-2 medium (Lonza, # EBM-2 cc-3154, EGM-2 singleQuots Supplements cc-4176) with added 1 % Pen/Strep for 14 days. For the isolation of tubular epithelial cells, the prepared cell suspension from the kidney sample was incubated with CD10-Microbeads (Miltenyi biotec # 130-093-452) and isolated using MACS. The isolated primary tubular epithelial cells were cultured in DMEM/F12 (1:1) + Glutamax (Gibco, # 31331) enriched with 10 % FCS and 1 % Pen/Strep for three weeks.

In order to immortalize the primary PDGFRβ$^+$, CD31$^+$ and CD10$^+$ cells, lentiviral particles SV40LT and HTERT were used. Lentiviral particles were produced by transient transfection of HEK293T cells using TransIT-LT (Mirus). Two types of amphotropic particles were generated by co-transfection of plasmids pBABE-puro-SV40-LT (Addgene 13970) or xlox-dNGFR-TERT (Addgene 69805) in combination with a packaging plasmid pUMVC (Addgene #8449) and a pseudotyping plasmid pMD2.G (Addgene 12259). Lentiviral particles were 100x concentrated using Lenti-X Concentrator (Clontech) 48 h post-transfection. Cell transduction was performed by incubating the target cells with serial dilutions of the retroviral supernatants (1:1 mix of concentrated particles containing SV40-LT or rather hTERT) for 48 h. Subsequently, the infected PDGFRβ$^+$, CD31$^+$ and CD10$^+$ cells were selected using 2 μg/mL puromycin at 72 h after transfection for 7 days.

4.4. Genetically fluorescent labeling PDGFRβ$^+$, endothelial and tubular epithelial cell lines

In order to trace the generated PDGFRβ$^+$, endothelial and tubular epithelial cell lines, RFP675 (red fluorescent protein 675), GFP (green fluorescent protein) and RFP (red fluorescent protein) were used. Three different retroviral particles for the three mentioned cell types were produced by transient transfection of HEK293T cells using TransIT-LT (Mirus). These three individual types of amphotropic particles were generated by co-transfection of plasmids RFP675 (Addgene 57824) or GFP (Addgene 57822) or RFP (Addgene 57823) in combination with a packaging plasmid pUMVC (Addgene 8449) and a pseudotyping plasmid pMD2.G (Addgene 12259). Retroviral particles were 100x concentrated using Retro-X concentrator (Clontech) 48 h post-transfection. Cell transduction was performed by incubating the target cells with the retroviral supernatants for 48 h. The transduced PDGFRβ$^+$, endothelial cells and tubular epithelial cells were cultured for 7 days in their indicated media. Consequently, the infected cells were sorted in the semi-purity mode targeting an efficiency of >80 % with the SONY SH800 sorter (Sony Biotechnology; 100 μm nozzle sorting chip Sony).

4.5. Immunofluorescence staining

The immunofluorescence staining was performed on monolayer cells or 3D-printed structures in glass 8 well chamber slides, μ- plate 96 well black, or culture plates (ibidi, 80827 and 89626, Greiner 12 well plate, 665180). After removal of the medium, the cells or 3D-constructs were washed with PBS (three times for 5 min) and fixed with 4 % formalin on ice for 5 min for cell monolayers, and 15–20 min for 3D constructs. Cells were incubated overnight with primary antibody in PBS +1 % BSA at 4 °C, washed 3 times for 5 min in PBS, and incubated with the secondary antibodies overnight at 4 °C. For imaging, constructs were left in PBS in their Ibidi/Greiner plate. Following DAPI (4′,6′-′diamidino-2-phenylindole) staining (Roche, 1:1000) the slides were mounted with Immu-Mount (Thermo scientific, # 9990402). Kidney tissues were fixed in 4 % (w/v) formalin for 2 h at RT, and frozen in OCT after dehydration in 30 % (w/v) sucrose overnight. The 5–10 μm cryosections were blocked in 5 % (v/v) donkey serum, and stained with primary antibody and secondary antibody for 60 and 45 min, respectively. These steps were followed by washing the sections with PBS (three times for 5 min). The sections were counterstained with DAPI (4′,6′-′diamidino-2-phenylindole) (Roche, 1:1000), washed in PBS and mounted with Immu-Mount (Thermo scientific, # 9990402). The following primary antibodies were used: human PDGFR beta (R&D System, MAB1263,1:100), human CD10 (Biolegend, 312214, 1:100), mouse-CD31(R&D System, AF3628, 1:100), human Fibronectin (Abcam, ab23750, 1:100), CD13 (Thermo Fisher, 11-0138-42, 1:100), POSTN(Sigma, HPA012306, 1:100), aSMA (R&D systems, MAB1420, 1:100), Col1a1(Biozol, 1310-01, 1:100), Cubilin (Sigma, HPA004133, 1:100), vWF (Sigma, HPA001815, 1:100), AF405 donkey anti-mouse (Dianova, 715-475-150, 1:200). The following secondary antibodies were used: AF488 donkey anti-goat (Dianova, 705-545-147, 1:100), AF488 donkey anti-mouse (Dianova, 715-545-151, 1:100), AF488 donkey anti-rabbit (Dianova, 711-545-152, 1:100), AF647 donkey anti-mouse (Dianova, 715-605-151, 1:100), AF647 donkey anti-rabbit (Dianova, 711-605-152, 1:100), Cy3 donkey anti-mouse (Dianova, 715-165-151, 1:100), AF405 donkey anti-goat (Dianova, 705-475-147, 1:200).

4.6. Immunohistochemistry

The immunohistochemistry was carried out on formalin-fixed, paraffin-embedded human kidney sections. The sections were incubated for 3–5 min in xylol, and dehydrated by incubating consecutively in ascending ethanol series (30, 50, 70 and 90 % (v/v)) with a final incubation in 100 % ethanol for 10 min. An antigen unmasking method was performed using the heating method (three times for 5 min), in which the sections were heated just below the boiling temperature in 10 mM sodium citrate buffer (Vektor, # H-3300), pH 6.0. After a washing step in water (three times for 5 min), blocking steps were performed by using 3 % (v/v) H2O2 (10 min), Avidin (10 min) and Biotin (10 min). The sections were stained with primary antibody and secondary antibody for 60 and 30 min, respectively. These steps were followed by washing the sections with PBS (three times for 5 min). After washing, sections were incubated with Ab-complex for 30 min at RT, followed by a washing step with PBS (three times for 5 min). Subsequently, the sections were incubated with DAB for 10 min, and were washed with ddH$_2$O (two times for 2 min). The nuclear staining was performed using Methyl Green (Vector laboratories, H-3402-500) for 2 min, followed by a dehydration step. The sections were mounted by Histokit. The following primary and secondary antibodies were used: human POSTN (Sigma, HPA012306, 1:100), human BHMT2 (Sigma, HPA044573, 1:500), goat-anti rabbit IgG (H + L), biotinylated (vector laboratories, BA1000, 1:300).

4.7. Live/dead staining

Human kidney -PDGFRβ$^+$, -CD31$^+$ and -CD10$^+$ cell lines were encapsulated in fibrinogen-gelatin hydrogels during the extrusion process using a 3D-Printer (Allevi2) for 24 or 72 h. The Live/Dead staining was conducted using Live/Dead Cell viability assay kit for mammalian cells (BioVision, #K502-100). Cell culture medium was removed carefully, and 0.5 mL staining solution was added to the hydrogels and incubated for 15 min at 37 °C. The staining solution is a combination of 2 μL of live cell staining dye, and 1 μL of dead cell staining dye in 1 mL of assay buffer. The confocal microscope X10 (Nikon A1R confocal microscope) was used to capture the complete depth of hydrogels and detect the live cells at Ex/Em = 485/530 [nm] and the dead cells at Ex/Em = 495/635 [nm].

4.8. Adipocyte differentiation and oil-red staining

3×10^5 PDGFRβ+ cells were cultured in 6 well plates. For this, the adipogenic base media (R&D systems, # CCM007) was used and the cells were incubated in a 37 °C and 5 % CO$_2$ incubator for 1–3 days. At 100 % confluency, the media was replaced with completed StemXVivo Adipogenic Differentiation Media to induce adipogenesis. Every 3–4 days, the medium was removed and replaced with the pre-warmed completed StemXVivo Adipogenic medium (R&D systems, #CCM007). The differentiation was completed after about 28 days, which was observed by morphological change, as well as visualization of the lipid vacuoles via an oil-red staining. In order to stain the lipid vacuoles in PDGFRβ$^+$ cells after differentiation, the medium was removed, and cells were washed with PBS. 2 mL of oil-red working solution (0.25 g Oil-red; Sigma-Aldrich #O0625, 50 mL isopropanol) was added and incubated at RT for 30 min. After removing the staining solution, cells were stained with Hematoxylin solution modified acc. to Gill II (Sigma, 1.05175.0500) for 10 min. After removal of Hematoxylin and washing 3 times with water, cells were exposed to bluing buffer (Dako, CS702) for 5 min. Cells were washed and kept on PBS while the red lipid vacuoles were visualized using a Leica DMR X microscope.

4.9. Chondrocytes differentiation and Alcian-blue staining

2.5×10^5 PDGFRβ+ cells were resuspended in 0.5 mL of the pre-warmed completed StemXVivo Chondrogenic Base Media (R&D systems, # CCM005). After centrifugation at 200×*g* for 5 min, the media was replaced with 0.5 mL of pre-warmed completed StemXVivo Chondrogenic differentiation media (R&D systems, # CCM006), and the cells were centrifuged again at 200×*g* for another 5 min. The medium was not removed, and the cap of the tube was loosened to allow the gas exchange. Tubes were incubated upright at 37 °C and 5 % CO_2 for the next 2 days. The media were replaced every 2 days with 0.5 mL of per-warmed completed StemXVivo Chondrogenic differentiation media. The 1–2 mm round-ball-pellet was harvested after differentiation at 28 days, and fixed through cryofixation. The cryo slides were ultimately used for Alcian-Blue staining (Abcam, # ab150662). Therefore, the cryo slides were incubated in acetic acid for 3 min, and then 30 min in Alcian-Blue, pH 2.5. After a wash step in water and staining in nuclear fast-red for 5 min, slides were rinsed in water and dehydrated. Slides were mounted and images were captured by Leica DMR X microscope.

4.10. Osteocytes differentiation; alkaline phosphatase activity and von-kossa staining

PDGFRβ$^+$ cells were cultured in a 6-well tissue culture dish using StemXVivo Osteogenic Base Media (R&D system, CCM007). At 70 % of confluency, this media was replaced with completed StemXvivo Osteogenic Differentiation media to induce osteogenesis. Every 3–4 days, the media was replaced with fresh StemXvivo Osteogenic Differentiation media (R&D system, # CCM009). After 28 days and observing morphological changes of cells, the dual alkaline phosphatase and von Kossa stainings were performed. Cells were fixed with 10 % cold Neutral Formalin Buffer (VWR, 10015-196) for 15 min, rinsed with distilled water, and left for 15 min in distilled water. To detect the alkaline phosphatase activity, samples were incubated for 45 min in the freshly prepared solution mixture of 0.005 g Naphthol (Sigma, N4875), 200 μl DMF (Fisher Scientific, D119-1), 25 mL Tris-HC (Sigma, 1082191000), pH:8.3, 25 mL distilled water, and 0.03 g red violet LB salt (Sigma, F338). This step was followed by 3–4 rinses in distilled water, and a staining with 2.5 % silver nitrate (Sigma, S8157) for 30 min. After silver staining, cells were rinsed in 60 % (v/v) isopropanol, and stained for 10 min with Hematoxylin solution modified acc. To Gill II (Sigma, 1.05175.0500). Tap water was used to wash the cells for 3 min, and bluing buffer (DAKO, CS702) was added for 5 min. Afterwards, cells were rinsed 3 times with distilled water, and finally covered with tap water. Images were captured by Leica DMR X microscope.

4.11. Quantitative measurement of calcium/protein

Calcium content in the differentiated PDGFRβ$^+$ cells was determined using a colorimetric *o*-cresolphthalein based assay (Randox Laboratories, Crumlin, UK). Cultured cells were washed and lysed in 0.1 M NaOH/0.1 % SDS. Cell lysates were transferred to the separate tubes. Subsequently, each well was washed with 200 μL 0.6 M HCl, and the collected fluid from each well was added to the respective tube. The preparation of the samples and the standard were performed according to the manufacturer's protocol in a 96-well plate (TPP Techno Plastic Products AG, Trasadingen, Switzerland), which was measured in a plate reader (FLUOstar OPTIMA, BMG LABTECH GmbH, Ortenberg, Germany) at 546 nm after 30 min.

4.12. Immunofluorescence and bright field imaging

Immunofluorescence images were acquired using a Nikon A1R confocal microscope with 10X and 20X objectives (Nikon), as well as a ZEISS Fluorescence microscope using 5X, 10X, 20X and 63X objectives. Trichrome/Masson stained sections were acquired using the Keyence microscope (BZ-9000) using 20X magnification. Von Kossa-alkaline phosphatase, oil red and chondrocytes stainings were analyzed using a Leica DMR X microscope using 10X, 20X and 40X magnifications. Raw imaging data was processed using Nikon Software, Keyence software, ImageJ or Qupath [71].

4.13. Electron microscopy

Samples were fixed in 3 % (w/v) glutaraldehyde (Agar scientific, Wetzlar, Germany), rinsed with 0.1 M sodium phosphate buffer (Merck, Darmstadt, Germany) and dehydrated by incubating consecutively in ascending ethanol series (30, 50, 70 and 90 % (v/v)), with a final incubation in 100 % ethanol for 3 × 10 min. After, samples were dried by critical point drying in liquid CO_2. Samples were coated with a 10 nm gold/palladium layer (Sputter Coater EM SCD500, Leica, Wetzlar, Germany). Microscopy was performed in a high vacuum environment at 10 kV acceleration voltage with an environmental scanning electron microscope (ESEM Philips XL30 FEG, FEI, Eindhoven, The Netherlands)

4.14. Quantitative RT-PCR

Cell pellets were harvested and washed with PBS, followed by RNA extraction according to the manufacturer's instructions using the RNeasy Mini Kit (Qiagen, 74106). The 3D-printed constructs were disintegrated by gently using a cell scratcher during the treatment with the RLT buffer according to the RNeasy Micro Kit (Qiagen, 74004) for extraction of RNA. 200 ng total RNA was reverse transcribed with High-Capacity cDNA Reverse Transcription Kit (Applied Biosystems). qRT-PCR was carried out with iTaq Universal SYBR Green Supermix (Bio-rad) and the Bio-Rad CFX96 Real Time System with the C1000 Touch Thermal Cycler. Cycling conditions were 95 °C for 3 min, then 40 cycles of 95 °C for 15 s and 60 °C for 1 min, followed by 1 cycle of 95 °C for 10 s. GAPDH was used as a housekeeping gene. Data were analyzed using the 2-CT method. The primers used are listed in Table 1.

4.15. Bulk RNA preparation

In this study we performed Bulk RNA sequencing for two experiments. The first experiment was designed to do a comprehensive characterization of the three generated human kidney cell lines (CD10, CD31, PDGFRβ), and to compare the similarity between cell lines to their human origin. The second experiment used human PDGFRβ$^+$ cells, which were treated w/wo TGFβ. The cells were cultivated in T-75 culture flasks and reached 60–70 % of confluency at the time of harvesting. Cell pellets were harvested and washed with PBS, followed by RNA extraction according to the manufacturer's instructions using the RNeasy Mini Kit (Qiagen, 74106). All experiments were performed in duplicates.

4.16. Human kidney fibrosis evaluation

Trichrome-Masson stained sections of the kidneys were analyzed and scored by taking pictures with Keyence microscope (BZ-9000), and the fibrosis area was measured with the Keyence analysis software program. The extent of interstitial fibrosis compared to the whole area was assessed as % of affected area.

Besides Masson's Trichrome staining, we stained for α-SMA and PDGFRβ as described above. Single and double positive cells were scored (by hand) in 5 high power fields (400x) per patient while glomeruli, arterioles and arteries were excluded based on morphology to include

Table 1
List of RT-PCR primer sequences (human).

Genes	Forward Primer	Reverse Primer
collagen type I alpha 1 chain	5‘-CCCAGCCACAAAGAGTCTACA	5‘-ATTGGTGGGATGTCTTCGTCT
fibronectin 1	5‘-AACAAACACTAATGTTAATTGCCCA	5‘-TCGGGAATCTTCTCTGTCAGC
actin alpha 2, smooth muscle	5‘-ACTGCCTTGGTGTGTGACAA	5‘-CACCATCACCCCCTGATGTC
gapdh	5‘- GAAGGTGAAGGTCGGAGTCA	5‘- TGGACTCCACGACGTACTCA
Kim1	5‘-CACAACAGATGGGAATGACACC	5“-TCCTTTAGTGGTATTGGCCGT

solely interstitial myofibroblasts.

4.17. Collagen1, αSMA, fibronectin protein expression evaluation

The 3D printed constructs were fixed with formalin and stained for collagen 1 antibody (as described in: immunofluorescence). For the 3D constructs, images containing 50 % tubular compartment and 50 % stromal compartment were then taken in 10x, 20x and 63x using Zeiss Fluorescence microscope. Using the Qupath Pixel classifier, we determined a threshold above which a pixel is positive and below which a pixel is negative for the marker. Equal areas between conditions were classified based on this threshold, and values were expressed as Positive Area in % of Collagen/αSMA/Fibronectin.

4.18. Bulk RNA-Seq data analyses

RNA-Seq preprocessing and quantification Bulk RNA-Seq data from the PDGFRβ$^+$, CD10$^+$ and CD31$^+$ cells, and PDGFRβ$^+$ cells treated w/wo TGFβ was analyzed using pipelines available in nf-core/rnaseq (version 2.7.2) [72] using standard parameters and based on version version 23.10.1-edge of nextflow [73]. For the read alignments, STAR (version 2.7.9a) [74] was used, and for quantification of reads Salmon (version 1.5.0) [75] was used, TrimGalore (version 0.6.6) used for the read trimming and for annotation of genes, GENCODE (version 38) was used [76]. The count matrix generated by Salmon was filtered, excluding genes labeled ‘Mt_tRNA,’ Mt_rRNA,’rRNA’ and ‘rRNA_pseudogene’ in the GENCODE annotation file. Subsequently, low expressed genes were excluded using the HTSFilter (1.42.0) [77].

4.19. Differential expression analyses (DEA)

Differential expression analysis was performed in R using the *DESeq* function of the DESeq2 (version 1.42.0) package [77], to identify the DEGs for specific comparisons. PCA was generated using the glmpca package in R. The p-value was corrected for multiple hypothesis correction and genes with corrected p-value ≤ 0.05 were considered as statistically significant.

4.20. Gene set enrichment analyses (GSEA)

Gene set enrichment analysis for each of the comparisons (TGFβ 72 h vs TGFβ 0 h, and TGFβ 24 h vs TGFβ 0 h) was performed with the clusterProfiler package v4.10.0 [78], using the *gseGO* function. GSEA was performed using “ALL” three ontologies (molecular function (MF), biological process (BP), and cellular component (CC)) provided in clusterProfiler. Gene sets enriched in up/down regulated genes were calculated using an ordered list of all differentially expressed genes sorted by logFC. The statistical significance was determined using adjusted p-value threshold of $\leq$ 0.05 after multiple test correction method bonferroni.

4.21. Progeny and Dorothea analysis (Functional analyses)

PROGENy version 1.24.0 was used to predict the signaling pathway activity in TGFβ 72 h vs TGFβ 0 h, and TGFβ 24 h vs TGFβ 0 h comparison, respectively [79] based on the top 100 responsive genes ranked by p-value. Pathway activity scores were estimated based on gene t-values obtained from DE-seq analysis as previously described [80]. DoRothEA (version 1.14.0), a collection of transcription factor targets was used with VIPER (version 1.36.0) to estimate the transcription factor activity using t-values obtained from DE-seq analysis [81,82] using VIPER.

4.22. Availability of analysis code and data

For reproducibility, the scripts for the computational analysis are accessible via GitHub https://github.com/hayatlab/kidney_bioprinting. The processed bulk RNA-Seq count matrices are available on zenodo at: 10.5281/zenodo.10973584.

4.23. RNA-seq analysis for characterization of human kidney cell lines

To ensure that the generated cell lines share similar gene-expression features with human kidney cells, we compared the gene expression profiles of the cell lines to the healthy human kidney single-cell transcriptomics data from Kuppe et al. [13]. Each cell line was compared to the rest of the bulk data to obtain differentially expressed genes. For the single-cell data, marker genes were obtained for each cell type using Seurat. Top genes with average logFC ≥ 1 and adjusted p-value (after multiple hypothesis correction) ≤ 0.05 were obtained and Jaccard similarity score (defined as jaccard similarity index*100) was computed on the overlapping genes from the bulk and the single-cell datasets.

4.24. 3D computer aided design

The construction of virtual objects was generated in computer-aided-design (CAD) software (Autodesk Inventor). Each virtual object was exported in stereolithography (STL) file format. The objects were then imported into the regenHU bioprinter-integrated BioCAM slicer software. The objects (tubule-like and interstitium) were then assigned to different printheads for the construct biofabrication. Two separate G-codes with two different designs were generated, for the printing of the 12-well plate and the 96-well plate constructs respectively.

4.25. Bioink preparation and bioprinting of 3D heterogeneous tissue constructs

The bioprinting was done with a regenHU 3DDiscovery bioprinter, or Allevi2. Unless otherwise stated, the bioinks and printing parameters were identical for the printing in both 12- and 96-well plates. To print two adjacent compartments within one construct, two bioink cell mixtures were prepared. To recreate the tubule-like structure, 4.10^5 cells/mL tubular epithelial cells were dispersed in the bioink material (bioink 1). The interstitium bioink contained 5.10^5 endothelial cells/mL combined with $2{,}5.10^5$ PDGFRβ$^+$ cells/mL (bioink 2). To achieve both bioinks, cell pellets were resuspended in 10 % gelatin (Sigma, G1890) dissolved in DMEM (Gibco, 11885084) + 5 % FBS + 1 % P/S. To the mixture of gelatin and cells, a 20 mg/mL fibrinogen solution in PBS (MILAN Analytica AG, # 001612) was added in a ratio of 3:1 to achieve a final concentration of 7.5 % gelatin and 5 mg/mL fibrinogen. The bioink components were mixed directly before printing at 37 °C degrees and immediately loaded in the designated syringe for each bioink. The preparation of the bioinks and loading of the syringes were done under sterile conditions. After loading, the syringes were incubated for 15 min at room temperature and placed into their respective preheated printheads (27 °C) on the bioprinter. The bioprinting process was run at a speed of 2 mm/s. Bioink 1 was printed with a flowrate of 0.09 μL/s and bioink 2 with a flowrate of 0.39 μL/s. Both bioinks were extruded through a 30 gauge nozzle (ID 0.150 mm, 12.7 mm length for printing in 12-well plates, 25.4 mm length for printing in 96-well plates). The printing took place either into Greiner 12-well plates (Greiner, 665180) or ibidi μ-Plate 96 Well Square Glass Bottom (Ibidi, 89627). The bioink remained stable in the syringe at 27 °C for at least 3 h, with minimal cell sedimentation. Immediately after printing, the construct was incubated at RT for 10 min before adding the crosslinking solution. The crosslinking solution composed of 1 mM HEPES (Thermo Fisher, 15630), 2.5 μM $CaCl_2$ (Sigma, 21115), 4 u Fibrogammin (CSL Behring, 1250) and 2.5 u Thrombin from human plasma (Sigma, T6884) per mL, and was activated for 15 min at 37 °C, but cooled down for 5 min at RT before adding to the constructs. The printed constructs were incubated with crosslinking solution for 30 min at RT and rinsed with PBS prior to adding cell media.

4.26. Measurement of the mechanical properties of the gel

The mechanical properties of hydrogels were determined using a TA Instruments Discovery HR-3 rheometer, equipped with a 20 mm diameter geometry with a cone angle of 2°. The measurements were performed with four replicates to ensure the reproducibility and reliability of the recorded data. Hydrogels were prepared by mixing gelatin and fibrinogen and cell culture media (at the ratio of 1:1:2), and 74 μL was placed in the center of the Peltier-plate using a viscous pipet (Mettler Toledo). To make sure that the geometry and hydrogel possess an integrated interface during measurement, the geometry was lowered to the measuring gap of 51 μm, a distance at which the gel is pressed down into the correct shape and then it was crosslinked on site. This was done by pipetting 1 mL of crosslinking solution (similar as used during bioprinting) around the sample to cover the surrounding of the gel. The system was left for 15 min to complete the crosslinking (similar time as used during bioprinting). After, the crosslinking medium was removed, and the sample was covered by a solvent trap to ensure it stays hydrated during the measurement. All measurements were performed at the constant temperature of 25 °C, running three programs of time sweep, amplitude sweep and a frequency sweep. The time sweep measurements were performed at the frequency of 1.0 Hz and a strain of 0.5 % for a total duration of 5 min. The data of the amplitude sweep was recorded for alternating strains between 0.1 % and 1000 % at a constant frequency of 1 Hz, while the frequency test was performed at the constant strain of 0.5 % for variable frequencies between 1 and 100 Hz.

4.27. Experiments in bioprinted construct TGFβ treatment experiment

TGFβ (100-21-10UG, Peprotech) 10 ng/mL was added to culture media, after a 24 h of serum starvation with 0.5 % FCS containing medium, to 70–80 % confluent PDGFRβ cells or 3D-printed constructs, respectively. To determine the effect of the deactivation of TGFβ, 10 μM SB431542 (STEMCELL Technologies, 72232) (or vehicle) was added to the culture wells. All experiments were performed in triplicates.

4.28. Ochratoxin A (OTA) treatment experiment

10 μM of mycotoxin ochratoxin A (R&D system, 1291) in DMSO was added to 70 % confluent tubular epithelial cells for 16 h. The control cells were treated with the same amount of DMSO without OTA. All experiments were performed in triplicates.

4.29. P-gp transporter assay

To confirm the presence of the renal efflux protein P-gp in our $CD10^+$ cells, the activity of the efflux transporter was measured by the amount of fluorescent calcein accumulation in the presence of a pump inhibitor. To that end, 0.01×10^6 cells were seeded in a clear bottom 96 ibidi plate. When the cells reached 95 % confluence after 2–3 days, cells were washed with Krebs Henseleit (KH) (Merck, K3753) buffer (PH 7.4). Cells were treated for 1 h with 5 μM P-gp transporter inhibitor PSC833 (Tocris Biosciences, Bristol, UK) in KH buffer at 37 °C, 5 % (v/v) CO_2, and afterwards exposed for 1 h to 1 μM Calcein-AM (Life Technologies Europe BV) with or without 5 μM PSC833 in KH buffer. After incubation, cells were washed 2 times with KH buffer before incubating for 45–60 min in 1 % Triton in KH buffer. Fluorescent read-out was determined in a plate reader using filter settings for excitation of 485 nm and emission of 530 nm. Data plotted is 3 technical replicates with each 12 biological replicates.

4.30. Supernatant transfer in vitro crosstalk studies

Constructs were bioprinted in a 96-well plate containing a) all three healthy cell types, (b) only the interstitial compartment, or (c) OTA pre-exposed $CD10^+$ cells in the tubular compartment without the interstitial compartment. In parallel, $CD10^+$ cells were exposed to 10 μM of OTA for 16 h, subsequently washed, and refreshed with 1:1 $PDGFR\beta^+$ and $CD31^+$ media for 24 h. This supernatant was harvested after 24 h, and on day 2 after printing, constructs were exposed to 200 μL of the supernatant. After 24 h, the supernatant of the bioprinted constructs was refreshed with new pre-exposed supernatant of the $CD10^+$ cells. After a total of 2.5 days of exposure, cells were fixed with 4 % PFA for 15 min on ice and proceeded to immunofluorescent staining as described above.

4.31. Human cytokine array

The Human Cytokine Array with 80 targets (Abcam, ab133998) was performed following the Abcam protocol using the same supernatant as described above. In short, membranes were blocked for 30 min at RT with 2 mL of 1X Blocking Buffer. After blocking, membranes were exposed to 1 mL of undiluted pre-exposed supernatant or control overnight at 4 °C while gently shaking. Membranes were washed in 20 mL of Wash Buffer I for 30 min, and washed 2x with 2 mL of Wash Buffer II for 5 min each. Next, membranes were incubated with 1X Biotin-Conjugated Anti-Cytokines at 4 °C overnight. After 3x 2 mL wash of Wash Buffer I, and 2x 2 mL wash of Wash Buffer II, the membranes were incubated with 1X HRP-Conjugated Streptavidin at 4 °C overnight. For chemiluminescence detection, membranes were washed as described after Biotin incubation and transferred to chromatography paper with 500 μL of detection buffer. Signal was detected using a Bio-Rad ChemiDoc MP Imaging System.

4.32. Statistical analysis

All data are expressed as mean ± s.d. Statistical analysis was performed using one-way ANOVA analysis followed by Tukey post-test or, when appropriate, an unpaired *t*-test with GraphPad Prism version 10.3.0. One asterisk was used to indicate significance with $P < 0.05$, whereas two asterisks were used to indicate significance with $P < 0.01$.

CRediT authorship contribution statement

Daphne Bouwens: Writing – review & editing, Writing – original draft, Investigation, Formal analysis. **Nazanin Kabgani:** Writing – original draft, Visualization, Methodology, Investigation, Conceptualization. **Cédric Bergerbit:** Investigation. **Hyojin Kim:** Visualization, Formal analysis, Data curation. **Susanne Ziegler:** Methodology. **Sadaf Ijaz:** Visualization, Formal analysis, Data curation. **Ali Abdallah:**

Formal analysis, Data curation. **Tamás Haraszti:** Investigation. **Sidrah Maryam:** Visualization, Formal analysis. **Abdolrahman Omidinia-Anarkoli:** Investigation. **Laura De Laporte:** Writing – review & editing, Conceptualization. **Sikander Hayat:** Writing – review & editing, Supervision, Conceptualization. **Jitske Jansen:** Writing – review & editing, Supervision, Conceptualization. **Rafael Kramann:** Writing – review & editing, Writing – original draft, Supervision, Methodology, Funding acquisition, Conceptualization.

Declaration of competing interest

The authors declare the following financial interests/personal relationships which may be considered as potential competing interests:

Rafael Kramann reports financial support was provided by German Research Foundation DFG SFBTRR219. Rafael Kramann reports financial support was provided by CRU344 4288578857858. Rafael Kramann reports financial support was provided by CRU5011 445703531. Rafael Kramann reports a relationship with Sequantrix GmbH that includes: board membership and equity or stocks. Sikander Hayat reports a relationship with Sequantrix GmbH that includes: board membership and equity or stocks. If there are other authors, they declare that they have no known competing financial interests or personal relationships that could have appeared to influence the work reported in this paper.

Acknowledgements

This work was supported by grants of the German Research Foundation (DFG: SFBTRR219) CRU344 4288578857858 and CRU5011 445703531, the BMBF eMed Consortia Fibromap and the BMBF Consortia CureFib and from Chugai Pharmaceuticals to RK and the EU POC 963675 Bioarchitecture to LDL. We thank Prof. Paul Kouwer for his valuable feedback on the rheology data.

Appendix A. Supplementary data

Supplementary data to this article can be found online at https://doi.org/10.1016/j.biomaterials.2024.123009.

Data availability

Data will be made available on request.

References

[1] V.A. Luyckx, M. Tonelli, J.W. Stanifer, The global burden of kidney disease and the sustainable development goals, Bull. World Health Organ. 96 (2018) 414–422D.

[2] W.G. Couser, G. Remuzzi, S. Mendis, M. Tonelli, The contribution of chronic kidney disease to the global burden of major noncommunicable diseases, Kidney Int. 80 (2011) 1258–1270.

[3] A.A. Seyhan, Lost in translation: the valley of death across preclinical and clinical divide – identification of problems and overcoming obstacles, Trans. Med. Commun. 4 (2019) 1–19.

[4] H. Wu, K. Uchimura, E.L. Donnelly, Y. Kirita, S.A. Morris, B.D. Humphreys, Comparative analysis and refinement of human PSC-derived kidney organoid differentiation with single-cell transcriptomics, Cell Stem Cell 23 (2018) 869–881.e8.

[5] M. Adler, S. Ramm, M. Hafner, J.L. Muhlich, E.M. Gottwald, E. Weber, A. Jaklic, A. K. Ajay, D. Svoboda, S. Auerbach, E.J. Kelly, J. Himmelfarb, V.S. Vaidya, A quantitative approach to screen for nephrotoxic compounds in vitro, J. Am. Soc. Nephrol. 27 (2016) 1015–1028.

[6] K.A. Homan, D.B. Kolesky, M.A. Skylar-Scott, J. Herrmann, H. Obuobi, A. Moisan, J.A. Lewis, Bioprinting of 3D convoluted renal proximal tubules on perfusable chips, Sci. Rep. 6 (2016) 34845.

[7] K.-J. Jang, A.P. Mehr, G.A. Hamilton, L.A. McPartlin, S. Chung, K.-Y. Suh, D. E. Ingber, Human kidney proximal tubule-on-a-chip for drug transport and nephrotoxicity assessment, Integr. Biol. 5 (2013) 1119–1129.

[8] A. Liu, X. Wang, X. Hu, Y. Deng, X. Wen, B. Lin, M. Zhou, W. Wang, Y. Luo, J. Deng, Q. Tang, X. Du, B. Qin, H. Song, H. Lin, Core fucosylation involvement in the paracrine regulation of proteinuria-induced renal interstitial fibrosis evaluated with the use of a microfluidic chip, Acta Biomater. 142 (2022) 99–112.

[9] S. Kim, J.-B. Lee, D. Kim, K. Kim, G.Y. Sung, Fabrication of nephrotoxic model by kidney-on-a-chip implementing renal proximal tubular function in vitro, BioChip J. 18 (2024) 477–484.

[10] M. Zhou, X. Zhang, X. Wen, T. Wu, W. Wang, M. Yang, J. Wang, M. Fang, B. Lin, H. Lin, Development of a functional glomerulus at the organ level on a chip to mimic hypertensive nephropathy, Sci. Rep. 6 (2016) 31771.

[11] Z. Li, L. Jiang, T. Tao, W. Su, Y. Guo, H. Yu, J. Qin, Assessment of cadmium-induced nephrotoxicity using a kidney-on-a-chip device, Toxicol. Res. 6 (2017) 372–380.

[12] N. Yamashita, R. Kramann, Mechanisms of kidney fibrosis and routes towards therapy, Trends Endocrinol. Metabol. 0 (2023), https://doi.org/10.1016/j.tem.2023.09.001.

[13] C. Kuppe, M.M. Ibrahim, J. Kranz, X. Zhang, S. Ziegler, J. Perales-Patón, J. Jansen, K.C. Reimer, J.R. Smith, R. Dobie, J.R. Wilson-Kanamori, M. Halder, Y. Xu, N. Kabgani, N. Kaesler, M. Klaus, L. Gernhold, V.G. Puelles, T.B. Huber, P. Boor, S. Menzel, R.M. Hoogenboezem, E.M.J. Bindels, J. Steffens, J. Floege, R. K. Schneider, J. Saez-Rodriguez, N.C. Henderson, R. Kramann, Decoding myofibroblast origins in human kidney fibrosis, Nature 589 (2021) 281–286.

[14] R. Kramann, J. Wongboonsin, M. Chang-Panesso, F.G. Machado, B.D. Humphreys, Gli1 pericyte loss induces capillary rarefaction and proximal tubular injury, J. Am. Soc. Nephrol. 28 (2017) 776–784.

[15] M. Takasato, P.X. Er, H.S. Chiu, M.H. Little, Generation of kidney organoids from human pluripotent stem cells, Nat. Protoc. 11 (2016) 1681–1692.

[16] Y. Xu, C. Kuppe, J. Perales-Patón, S. Hayat, J. Kranz, A.T. Abdallah, J. Nagai, Z. Li, F. Peisker, T. Saritas, M. Halder, S. Menzel, K. Hoeft, A. Kenter, H. Kim, C.R.C. van Roeyen, M. Lehrke, J. Moellmann, T. Speer, E.M. Buhl, R. Hoogenboezem, P. Boor, J. Jansen, C. Knopp, I. Kurth, B. Smeets, E. Bindels, M.E.J. Reinders, C. Baan, J. Gribnau, E.J. Hoorn, J. Steffens, T.B. Huber, I. Costa, J. Floege, R.K. Schneider, J. Saez-Rodriguez, B.S. Freedman, R. Kramann, Adult human kidney organoids originate from CD24 cells and represent an advanced model for adult polycystic kidney disease, Nat. Genet. 54 (2022) 1690–1701.

[17] J.O. Aceves, S. Heja, K. Kobayashi, S.S. Robinson, T. Miyoshi, T. Matsumoto, O.J. M. Schäffers, R. Morizane, J.A. Lewis, 3D proximal tubule-on-chip model derived from kidney organoids with improved drug uptake, Sci. Rep. 12 (2022) 1–14.

[18] R. Kramann, R.K. Schneider, D.P. DiRocco, F. Machado, S. Fleig, P.A. Bondzie, J. M. Henderson, B.L. Ebert, B.D. Humphreys, Perivascular Gli1+ progenitors are key contributors to injury-induced organ fibrosis, Cell Stem Cell 16 (2015) 51–66.

[19] N. Yamashita, T. Kusaba, T. Nakata, A. Tomita, T. Ida, N. Watanabe-Uehara, K. Ikeda, T. Kitani, M. Uehara, Y. Kirita, S. Matoba, B.D. Humphreys, K. Tamagaki, Intratubular epithelial-mesenchymal transition and tubular atrophy after kidney injury in mice, Am. J. Physiol. Ren. Physiol. 319 (2020) F579–F591.

[20] S. Lovisa, V.S. LeBleu, B. Tampe, H. Sugimoto, K. Vadnagara, J.L. Carstens, C.-C. Wu, Y. Hagos, B.C. Burckhardt, T. Pentcheva-Hoang, H. Nischal, J.P. Allison, M. Zeisberg, R. Kalluri, Epithelial-to-mesenchymal transition induces cell cycle arrest and parenchymal damage in renal fibrosis, Nat. Med. 21 (2015) 998–1009.

[21] B.M. Rush, S.A. Small, D.B. Stolz, R.J. Tan, An efficient sieving method to isolate intact glomeruli from adult rat kidney, J. Vis. Exp. (2018), https://doi.org/10.3791/58162.

[22] A. Bera, F. Das, N. Ghosh-Choudhury, X. Li, S. Pal, Y. Gorin, B.S. Kasinath, H. E. Abboud, G. Ghosh Choudhury, A positive feedback loop involving Erk5 and Akt turns on mesangial cell proliferation in response to PDGF, Am. J. Physiol. Cell Physiol. 306 (2014) C1089–C1100.

[23] R. Kramann, S.V. Fleig, R.K. Schneider, S.L. Fabian, D.P. DiRocco, O. Maarouf, J. Wongboonsin, Y. Ikeda, D. Heckl, S.L. Chang, H.G. Rennke, S.S. Waikar, B. D. Humphreys, Pharmacological GLI2 inhibition prevents myofibroblast cell-cycle progression and reduces kidney fibrosis, J. Clin. Invest. 125 (2015) 2935–2951.

[24] M. D'Urso, N.A. Kurniawan, Mechanical and physical regulation of fibroblast-myofibroblast transition: from cellular mechanoresponse to tissue pathology, Front. Bioeng. Biotechnol. 8 (2020) 609653.

[25] Q. Zhao, T. Shao, Y. Zhu, G. Zong, J. Zhang, S. Tang, Y. Lin, H. Ma, Z. Jiang, Y. Xu, X. Wu, T. Zhang, An MRTF-A-ZEB1-IRF9 axis contributes to fibroblast-myofibroblast transition and renal fibrosis, Exp. Mol. Med. 55 (2023) 987–998.

[26] M. Mael-Ainin, A. Abed, S.J. Conway, J.-C. Dussaule, C. Chatziantoniou, Inhibition of periostin expression protects against the development of renal inflammation and fibrosis, J. Am. Soc. Nephrol. 25 (2014) 1724–1736.

[27] J.H. Hwang, S.H. Yang, Y.C. Kim, J.H. Kim, J.N. An, K.C. Moon, Y.K. Oh, J.Y. Park, D.K. Kim, Y.S. Kim, C.S. Lim, J.P. Lee, Experimental inhibition of periostin attenuates kidney fibrosis, Am. J. Nephrol. 46 (2017) 501–517.

[28] J.N. An, S.H. Yang, Y.C. Kim, J.H. Hwang, J.Y. Park, D.K. Kim, J.H. Kim, D.W. Kim, D.G. Hur, Y.K. Oh, C.S. Lim, Y.S. Kim, J.P. Lee, Periostin induces kidney fibrosis after acute kidney injury via the p38 MAPK pathway, Am. J. Physiol. Ren. Physiol. 316 (2019) F426–F437.

[29] G. Serini, M.L. Bochaton-Piallat, P. Ropraz, A. Geinoz, L. Borsi, L. Zardi, G. Gabbiani, The fibronectin domain ED-A is crucial for myofibroblastic phenotype induction by transforming growth factor-beta1, J. Cell Biol. 142 (1998) 873–881.

[30] A.F. Muro, F.A. Moretti, B.B. Moore, M. Yan, R.G. Atrasz, C.A. Wilke, K.R. Flaherty, F.J. Martinez, J.L. Tsui, D. Sheppard, F.E. Baralle, G.B. Toews, E.S. White, An essential role for fibronectin extra type III domain A in pulmonary fibrosis, Am. J. Respir. Crit. Care Med. 177 (2008) 638–645.

[31] M. Polonsky, L.M.S. Gerhardt, J. Yun, K. Koppitch, K.L. Colón, H. Amrhein, S. Zheng, G.-C. Yuan, M. Thomson, L. Cai, A.P. McMahon, Spatial transcriptomics defines injury-specific microenvironments in the adult mouse kidney and novel cellular interactions in regeneration and disease, bioRxiv (2023), https://doi.org/10.1101/2023.11.22.568217.

[32] M.J. Lee, M.R. Lee, Y.B. Choi, J.T. Park, S.H. Han, T.-H. Yoo, S.-W. Kang, H.J. Kim, Fp021insulin-like growth factor binding protein 3 specific DNA aptamer

attenuated renal tubular fibrosis, Nephrol. Dial. Transplant. 34 (2019), https://doi.org/10.1093/ndt/gfz106.fp021.
[33] L. Valiño-Rivas, L. Cuarental, M.I. Ceballos, A. Pintor-Chocano, M.V. Perez-Gomez, A.B. Sanz, A. Ortiz, M.D. Sanchez-Niño, Growth differentiation factor-15 preserves Klotho expression in acute kidney injury and kidney fibrosis, Kidney Int. 101 (2022) 1200–1215.
[34] Z. Cheng, X. Zhang, Y. Zhang, L. Li, P. Chen, Role of MMP-2 and CD147 in kidney fibrosis, Open Life Sci. 17 (2022) 1182–1190.
[35] H. Zhao, Y. Dong, X. Tian, T.K. Tan, Z. Liu, Y. Zhao, Y. Zhang, D.C. Harris, G. Zheng, Matrix metalloproteinases contribute to kidney fibrosis in chronic kidney diseases, World J. Nephrol. 2 (2013) 84–89.
[36] L. Chen, X. Li, Y. Deng, J. Chen, M. Huang, F. Zhu, Z. Gao, L. Wu, Q. Hong, Z. Feng, G. Cai, X. Sun, X. Bai, X. Chen, The PI3K-Akt-mTOR pathway mediates renal pericyte-myofibroblast transition by enhancing glycolysis through HKII, J. Transl. Med. 21 (2023) 323.
[37] R. Cao, W. Su, J. Sheng, Y. Guo, J. Su, C. Zhang, H. Wang, Y. Tang, L. Chen, R. Qiao, X. Chen, X. Huang, Y. Zhou, L. Zhu, Z. Bai, X. Zhang, J.-A. Gustafsson, Q. Wan, H.-Y. Lan, Y. Guan, Estrogen receptor β attenuates renal fibrosis by suppressing the transcriptional activity of Smad3, Biochim. Biophys. Acta, Mol. Basis Dis. 1869 (2023) 166755.
[38] Estradiol reverses renal injury in Alb/TGF-β1 transgenic mice, Kidney Int. 66 (2004) 2148–2154.
[39] X. Liang, D.M. Potenza, A. Brenna, Y. Ma, Z. Ren, X. Cheng, X.-F. Ming, Z. Yang, Hypoxia induces renal epithelial injury and activates fibrotic signaling through up-regulation of arginase-II, Front. Physiol. 12 (2021) 773719.
[40] S. Tanaka, T. Tanaka, M. Nangaku, Hypoxia as a key player in the AKI-to-CKD transition, Am. J. Physiol. Ren. Physiol. 307 (2014) F1187–F1195.
[41] M.E. Choi, Y. Ding, S.I. Kim, TGF-β signaling via TAK1 pathway: role in kidney fibrosis, Semin. Nephrol. 32 (2012) 244–252.
[42] O.H. Maarouf, A. Aravamudhan, D. Rangarajan, T. Kusaba, V. Zhang, J. Welborn, D. Gauvin, X. Hou, R. Kramann, B.D. Humphreys, Paracrine Wnt1 drives interstitial fibrosis without inflammation by tubulointerstitial cross-talk, J. Am. Soc. Nephrol. 27 (2016) 781–790.
[43] S.P. Higgins, Y. Tang, C.E. Higgins, B. Mian, W. Zhang, R.-P. Czekay, R. Samarakoon, D.J. Conti, P.J. Higgins, TGF-β1/p53 signaling in renal fibrogenesis, Cell. Signal. 43 (2018) 1–10.
[44] N. Frangogiannis, Transforming growth factor-β in tissue fibrosis, J. Exp. Med. 217 (2020) e20190103.
[45] D. Liang, Z. Li, Z. Feng, Z. Yuan, Y. Dai, X. Wu, F. Zhang, Y. Wang, Y. Zhou, L. Liu, M. Shi, Y. Xiao, B. Guo, Metformin improves the senescence of renal tubular epithelial cells in a high-glucose state through E2F1, Front. Pharmacol. 13 (2022) 926211.
[46] S. Song, X. Zhang, Z. Huang, Y. Zhao, S. Lu, L. Zeng, F. Cai, T. Wang, Z. Pei, X. Weng, W. Luo, H. Lu, Z. Wei, J. Wu, P. Yu, L. Shen, X. Zhang, A. Sun, J. Ge, TEA domain transcription factor 1(TEAD1) induces cardiac fibroblasts cells remodeling through BRD4/Wnt4 pathway, Signal Transduct. Targeted Ther. 9 (2024) 45.
[47] F. Peisker, M. Halder, J. Nagai, S. Ziegler, N. Kaesler, K. Hoeft, R. Li, E.M.J. Bindels, C. Kuppe, J. Moellmann, M. Lehrke, C. Stoppe, M.T. Schaub, R.K. Schneider, I. Costa, R. Kramann, Mapping the cardiac vascular niche in heart failure, Nat. Commun. 13 (2022) 3027.
[48] S.G. Szeto, M. Narimatsu, M. Lu, X. He, A.M. Sidiqi, M.F. Tolosa, L. Chan, K. De Freitas, J.F. Bialik, S. Majumder, S. Boo, B. Hinz, Q. Dan, A. Advani, R. John, J. L. Wrana, A. Kapus, D.A. Yuen, YAP/TAZ are mechanoregulators of TGF–smad signaling and renal fibrogenesis, J. Am. Soc. Nephrol. 27 (2016) 3117–3128.
[49] P.S. Gungor-Ozkerim, I. Inci, Y.S. Zhang, A. Khademhosseini, M.R. Dokmeci, Bioinks for 3D bioprinting: an overview, Biomater. Sci. 6 (2018) 915–946.
[50] A. Rossi, T. Pescara, A.M. Gambelli, F. Gaggia, A. Asthana, Q. Perrier, G. Basta, M. Moretti, N. Senin, F. Rossi, G. Orlando, R. Calafiore, Biomaterials for extrusion-based bioprinting and biomedical applications, Front. Bioeng. Biotechnol. 12 (2024) 1393641.
[51] J. Zhu, R.E. Marchant, Design properties of hydrogel tissue-engineering scaffolds, Expet Rev. Med. Dev. 8 (2011) 607–626, https://doi.org/10.1586/erd.11.27.
[52] S. Sakai, K. Hirose, K. Taguchi, Y. Ogushi, K. Kawakami, An injectable, in situ enzymatically gellable, gelatin derivative for drug delivery and tissue engineering, Biomaterials 30 (2009) 3371–3377.
[53] T. Rajangam, S.S.A. An, Fibrinogen and fibrin based micro and nano scaffolds incorporated with drugs, proteins, cells and genes for therapeutic biomedical applications, Int. J. Nanomed. 8 (2013) 3641–3662.
[54] Y. Li, H. Meng, Y. Liu, B.P. Lee, Fibrin Gel as an Injectable Biodegradable Scaffold and Cell Carrier for Tissue Engineering, ScientificWorldJournal 2015, 2015 685690.
[55] A.S. Wolberg, Thrombin generation and fibrin clot structure, Blood Rev. 21 (2007) 131–142, https://doi.org/10.1016/j.blre.2006.11.001.
[56] F. Schreibing, R. Kramann, Mapping the human kidney using single-cell genomics, Nat. Rev. Nephrol. 18 (2022) 347–360.
[57] R. Kramann, D.P. DiRocco, B.D. Humphreys, Understanding the origin, activation and regulation of matrix-producing myofibroblasts for treatment of fibrotic disease, J. Pathol. 231 (2013) 273–289.
[58] C.-S. Khoi, J.-H. Chen, T.-Y. Lin, C.-K. Chiang, K.-Y. Hung, Ochratoxin A-induced nephrotoxicity: up-to-date evidence, Int. J. Mol. Sci. 22 (2021), https://doi.org/10.3390/ijms222011237.
[59] W. Chen, H. Yuan, W. Cao, T. Wang, W. Chen, H. Yu, Y. Fu, B. Jiang, H. Zhou, H. Guo, X. Zhao, Blocking interleukin-6 trans-signaling protects against renal fibrosis by suppressing STAT3 activation, Theranostics 9 (2019) 3980–3991.
[60] Z. Wang, K. Famulski, J. Lee, S.K. Das, X. Wang, P. Halloran, G.Y. Oudit, Z. Kassiri, TIMP2 and TIMP3 have divergent roles in early renal tubulointerstitial injury, Kidney Int. 85 (2014) 82–93.
[61] K.H. Yoo, B.A. Thornhill, M.S. Forbes, C.M. Coleman, E.S. Marcinko, L. Liaw, R. L. Chevalier, Osteopontin regulates renal apoptosis and interstitial fibrosis in neonatal chronic unilateral ureteral obstruction, Kidney Int. 70 (2006) 1735–1741.
[62] S.K. Sinha, M. Mellody, M.B. Carpio, R. Damoiseaux, S.B. Nicholas, Osteopontin as a biomarker in chronic kidney disease, Biomedicines 11 (2023), https://doi.org/10.3390/biomedicines11051356.
[63] M.A. Venkatachalam, J.M. Weinberg, W. Kriz, A.K. Bidani, Failed tubule recovery, AKI-CKD transition, and kidney disease progression, J. Am. Soc. Nephrol. 26 (2015) 1765–1776.
[64] D.A. Ferenbach, J.V. Bonventre, Mechanisms of maladaptive repair after AKI leading to accelerated kidney ageing and CKD, Nat. Rev. Nephrol. 11 (2015) 264–276.
[65] K.A. Nath, Tubulointerstitial changes as a major determinant in the progression of renal damage, Am. J. Kidney Dis. 20 (1992) 1–17.
[66] R. Kramann, M. Tanaka, B.D. Humphreys, Fluorescence microangiography for quantitative assessment of peritubular capillary changes after AKI in mice, J. Am. Soc. Nephrol. 25 (2014) 1924–1931.
[67] D.P. Basile, The endothelial cell in ischemic acute kidney injury: implications for acute and chronic function, Kidney Int. 72 (2007) 151–156.
[68] C. Jensen, Y. Teng, Is it time to start transitioning from 2D to 3D cell culture? Front. Mol. Biosci. 7 (2020) 33.
[69] T.M. DesRochers, L. Suter, A. Roth, D.L. Kaplan, Bioengineered 3D human kidney tissue, a platform for the determination of nephrotoxicity, PLoS One 8 (2013) e59219.
[70] A.I. Astashkina, B.K. Mann, G.D. Prestwich, D.W. Grainger, Comparing predictive drug nephrotoxicity biomarkers in kidney 3-D primary organoid culture and immortalized cell lines, Biomaterials 33 (2012) 4712–4721.
[71] P. Bankhead, M.B. Loughrey, J.A. Fernández, Y. Dombrowski, D.G. McArt, P. D. Dunne, S. McQuaid, R.T. Gray, L.J. Murray, H.G. Coleman, J.A. James, M. Salto-Tellez, P.W. Hamilton, QuPath: open source software for digital pathology image analysis, Sci. Rep. 7 (2017) 16878.
[72] P.A. Ewels, A. Peltzer, S. Fillinger, H. Patel, J. Alneberg, A. Wilm, M.U. Garcia, P. Di Tommaso, S. Nahnsen, The nf-core framework for community-curated bioinformatics pipelines, Nat. Biotechnol. 38 (2020) 276–278.
[73] Website, Harshil Patel, Phil Ewels, Alexander Peltzer, Rickard Hammarén, Olga Botvinnik, Gregor Sturm, … Colin Davenport, Zenodo, 2021, https://doi.org/10.5281/zenodo.4757022. nf-core/rnaseq: nf-core/rnaseq v3.0 - Lead Alligator (Version 3.0).
[74] A. Dobin, C.A. Davis, F. Schlesinger, J. Drenkow, C. Zaleski, S. Jha, P. Batut, M. Chaisson, T.R. Gingeras, STAR: ultrafast universal RNA-seq aligner, Bioinformatics 29 (2013) 15–21.
[75] R. Patro, G. Duggal, M.I. Love, R.A. Irizarry, C. Kingsford, Salmon provides fast and bias-aware quantification of transcript expression, Nat. Methods 14 (2017) 417–419.
[76] A. Rau, M. Gallopin, G. Celeux, F. Jaffrézic, Data-based filtering for replicated high-throughput transcriptome sequencing experiments, Bioinformatics 29 (2013) 2146–2152.
[77] M.I. Love, W. Huber, S. Anders, Moderated estimation of fold change and dispersion for RNA-seq data with DESeq2, Genome Biol. 15 (2014) 550.
[78] T. Wu, E. Hu, S. Xu, M. Chen, P. Guo, Z. Dai, T. Feng, L. Zhou, W. Tang, L. Zhan, X. Fu, S. Liu, X. Bo, G. Yu, clusterProfiler 4.0: a universal enrichment tool for interpreting omics data, Innovation 2 (2021) 100141.
[79] M. Schubert, B. Klinger, M. Klünemann, A. Sieber, F. Uhlitz, S. Sauer, M.J. Garnett, N. Blüthgen, J. Saez-Rodriguez, Perturbation-response genes reveal signaling footprints in cancer gene expression, Nat. Commun. 9 (2018) 20.
[80] K. Hoeft, G.J.L. Schaefer, H. Kim, D. Schumacher, T. Bleckwehl, Q. Long, B. M. Klinkhammer, F. Peisker, L. Koch, J. Nagai, M. Halder, S. Ziegler, E. Liehn, C. Kuppe, J. Kranz, S. Menzel, I. Costa, A. Wahida, P. Boor, R.K. Schneider, S. Hayat, R. Kramann, Platelet-instructed SPP1+ macrophages drive myofibroblast activation in fibrosis in a CXCL4-dependent manner, Cell Rep. 42 (2023) 112131.
[81] L. Garcia-Alonso, C.H. Holland, M.M. Ibrahim, D. Turei, J. Saez-Rodriguez, Benchmark and integration of resources for the estimation of human transcription factor activities, Genome Res. 29 (2019) 1363–1375.
[82] P. Badia-i-Mompel, J. Vélez Santiago, J. Braunger, C. Geiss, D. Dimitrov, S. Müller-Dott, P. Taus, A. Dugourd, C.H. Holland, R.O. Ramirez Flores, J. Saez-Rodriguez, decoupleR: ensemble of computational methods to infer biological activities from omics data, Bioinform. Advan. 2 (2022) vbac016.

Update

Biomaterials

Volume 317, Issue , June 2025, Page

DOI: https://doi.org/10.1016/j.biomaterials.2024.123070

Biomaterials 317 (2025) 123070

Contents lists available at ScienceDirect

Biomaterials

journal homepage: www.elsevier.com/locate/biomaterials

Corrigendum

Corrigendum to “A bioprinted and scalable model of human tubulo-interstitial kidney fibrosis” [Biomaterials, 316 (2025) 123009]

Daphne Bouwens [a,1], Nazanin Kabgani [a,1], Cédric Bergerbit [d,e,2], Hyojin Kim [a,2], Susanne Ziegler [a], Sadaf Ijaz [a], Ali Abdallah [b], Tamás Haraszti [c,d], Sidrah Maryam [a], Abdolrahman Omidinia-Anarkoli [d,e], Laura De Laporte [c,d,e], Sikander Hayat [a], Jitske Jansen [a], Rafael Kramann [a,f,*]

[a] Department of Medicine 2 (Nephrology, Rheumatology, Clinical Immunology, Hypertension), RWTH Aachen University Medical Faculty, Aachen, Germany
[b] Interdisciplinary Center for Clinical Research, RWTH University Aachen, Germany
[c] ITMC-Institute for Technical and Macromolecular Chemistry, RWTH Aachen University, Aachen, Germany
[d] DWI-Leibniz Institute for Interactive Materials e.V., Aachen, Germany
[e] AMB-Advanced Materials for Biomedicine, Institute of Applied Medical Engineering, University Hospital Aachen, Germany
[f] Department of Internal Medicine, Nephrology and Transplantation, Erasmus Medical Center, Rotterdam, the Netherlands

The authors regret that the labelling of shared authors is incorrect. Jansen and Kramann are shared senior authors, Bergerbit and Kim not. Bergerbit and Kim contributed equally but are not shared senior authors. Please find below the correct labelling:

Daphne Bouwens [a,1], Nazanin Kabgani [a,1], Cédric Bergerbit [d,e,2], Hyojin Kima,[2], Susanne Ziegler[a], Sadaf Ijaz[a], Ali Abdallah [b], Tamás Haraszti[c,d], Sidrah Maryam[a], Abdolrahman Omidinia-Anarkoli[d,e], Laura De Laporte[c,d,e], Sikander Hayat[a], Jitske Jansen[a,3], Rafael Kramann[a,f,3,*]

[a]Department of Medicine 2 (Nephrology, Rheumatology, Clinical Immunology, Hypertension), RWTH Aachen University Medical Faculty, Aachen, Germany.

[b]Interdisciplinary Center for Clinical Research, RWTH University Aachen, Germany.

[c]ITMC-Institute for Technical and Macromolecular Chemistry, RWTH Aachen University, Aachen, Germany; DWI-Leibniz Institute for Interactive Materials e.V., Aachen, Germany.

[d]DWI-Leibniz Institute for Interactive Materials e.V., Aachen, Germany; AMB-Advanced Materials for Biomedicine, Institute of Applied Medical Engineering, University Hospital Aachen, Germany.

[e]AMB-Advanced Materials for Biomedicine, Institute of Applied Medical Engineering, University Hospital Aachen, Germany.

[f]Department of Internal Medicine, Nephrology and Transplantation, Erasmus Medical Center, Rotterdam, the Netherlands. Electronic address: rkramann@gmx.net.

*Corresponding author. Department of Medicine 2 RWTH Aachen University, Medical Faculty, Pauwelsstrasse 30, 52074, Aachen, Germany. E mail address: rkramann@gmx.net (R. Kramann).

[1] Both authors contributed equally.

[2] Both authors contributed equally.

[3] Shared senior authors.

The authors would like to apologise for any inconvenience caused.

DOI of original article: https://doi.org/10.1016/j.biomaterials.2024.123009.

* Corresponding author. Department of Medicine 2 RWTH Aachen University, Medical Faculty, Pauwelsstrasse 30, 52074, Aachen, Germany.
E-mail address: rkramann@gmx.net (R. Kramann).

[1] Both authors contributed equally.

[2] Shared senior authors.

https://doi.org/10.1016/j.biomaterials.2024.123070